
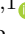





CALISYM: Learning Symplectic Dynamics of Real-World Systems through Structured Canonical Lifts

Aristotelis Papatheodorou^{*,1}  Pranav Vaidhyathanan^{*,1} 
 Natalia Ares¹  Ioannis Havoutis¹  Gerard J. Milburn² 

Abstract—Physics-informed learning promises data-efficient and stable dynamics prediction, yet its strongest geometric guarantees have largely remained confined to closed conservative systems. This excludes many robotic systems of practical interest, where actuation, dissipation, and constraints continuously exchange energy and momentum with the environment. We introduce CALISYM[†], a lightweight framework that extends exact symplectic learning to such systems by changing where the geometric prior is imposed. Rather than enforcing symplecticity on the measured physical state, CALISYM embeds the state and its physical ports into a structured lifted canonical phase space, where the learned dynamics evolve through an exactly symplectic map. The lift is explicit and algebraic, requiring neither recurrent latent states, transformer decoders, implicit optimization, nor inference-time ODE integration. We instantiate the framework with generalized-ridge SYMPNET predictors and introduce GRB-SYMPNET, a B-spline variant that combines local approximation with exact symplectic structure. Experiments on a controlled dissipative double pendulum, a real-world quadrotor, and a contact-rich quadruped demonstrate consistent improvements in out-of-distribution autoregressive prediction while using parameter-efficient models. At the same time, the learned lifted dynamics preserve the symplectic form to numerical precision. These results show that symplectic learning can be extended beyond conservative mechanics through structured canonical lifts, enabling geometry-preserving dynamics models for real-world robotic systems.

Index Terms—robot dynamics learning, symplectic neural networks, geometric machine learning, structure-preserving learning, Hamiltonian systems, contact-rich robotics, model-based control.

I. INTRODUCTION

DYNAMICS has been studied extensively, producing a wide range of methods for explaining, predicting, and controlling the physical systems around us. The arrival of computation extended that reach to systems of scale and complexity that no closed-form analysis could touch. Amongst other fields, this shift has been highly consequential for robotics, where accurate dynamics models now underpin nearly every aspect of estimation, prediction and control. However, accuracy almost always comes with a cost.

¹Aristotelis Papatheodorou, Pranav Vaidhyathanan, Natalia Ares and Ioannis Havoutis are with the Department of Engineering Science, University of Oxford, Oxford, UK. A.P. is supported by Oxford’s Clarendon Fund and the JPMorgan Chase AI PhD Fellowship. P.V. is supported by the United States Army Research Office under Award No. W911NF-21-S-0009-2. N.A. acknowledges support from the European Research Council (Grant agreement 948932) and the Royal Society (URF-R1-191150).

²School of Mathematics and Physics, University of Sussex, Brighton, BN1 9RH, UK. National Centre for Quantum Computing, Rutherford Appleton Laboratory, Harwell Campus, Didcot, Oxfordshire, OX11 0QX UK

*Equal Contribution {aristotelis, pranav}@robots.ox.ac.uk

[†]Open-source implementation will be released upon acceptance.

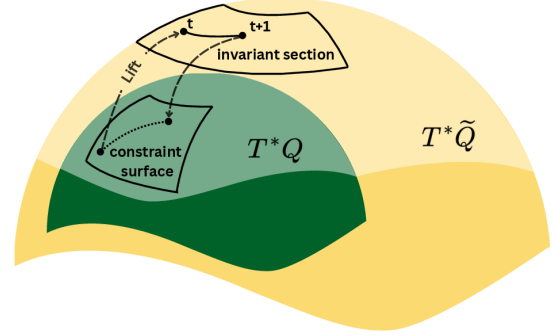


Fig. 1. Overview of CALISYM. The measured state lives in the physical phase space T^*Q , the cotangent bundle of the configuration manifold Q . Because the system exchanges energy and impulses through actuation, and contact, the physical dynamics on T^*Q need not be closed or symplectic. CALISYM therefore embeds the physical state $x_t = (q_t, p_t)$ and its current ports e_t into a gauge-fixed data section S_{e_t} of the lifted phase space $T^*\tilde{Q}$. An exactly symplectic map $\Phi_\theta^{\Delta t}$ advances the lifted state from z_t to z_{t+1} , after which the prediction is projected back to the physical state $\hat{x}_{t+1} = \Pi_{\mathcal{X}}(z_{t+1})$. For autoregressive rollout, the prediction is re-embedded with the next port value through $z_{t+1} = \sigma_{e_{t+1}}(\hat{x}_{t+1})$. Thus, symplecticity is enforced in $T^*\tilde{Q}$, while the projected physical dynamics on T^*Q may remain forced, dissipative, or contact-rich.

Classical model-based control [1], [2] rests on first-principles descriptions of the system, such as rigid-body mechanics, contact models, and actuator dynamics [3]. Yet these descriptions face two limits at once, one computational and one more fundamental. The computational limit surfaces in methods such as model-predictive control [4] and state estimation [5], which must repeatedly query the underlying model. High-fidelity models are often too expensive to evaluate at control rates, leading practitioners toward elaborate hand-engineered models [6], [7] or coarse simplifications that widen the simulation-to-reality gap [8]. The second limitation is more fundamental. Clean analytical models capture the dominant inertial, gravitational, and Coriolis effects, but high-performance robots operate precisely where neglected effects matter [9]. Aerial robots face thrust limits and aerodynamic drag [10], while legged robots face friction, compliance, impacts, and intermittent contact [11]. These are exactly the non-conservative effects that are hardest to derive from first principles and, as we will argue, the ones that most strongly violate the assumptions behind today’s most reliable learned models [12]–[15].

With the emergence of data-driven methods, predicting dynamics has shifted from hand-derived equations toward learned world models [16], i.e., neural predictors trained to roll out of the future state of a system directly from data. In

model-based reinforcement learning [17], [18], such models are no longer passive simulators but are queried in closed loop, generating the imagined trajectories on which planning and policy optimization depend [19]. Their promise is speed without the brittleness of hand-tuned simplifications, with a single forward pass replacing an expensive solve. Their peril is that a learned map can be arbitrary. Small single-step errors compound over a rollout, and without any constraint grounding the prediction to the underlying physics, long-horizon trajectories drift and violate conservation laws the real system obeys. Their performance degradation is only amplified if we consider distributions shifts and conditions out of their nominal training scenarios [20].

This is the gap physics-informed learning sets out to close [21], [22]. Rather than being left to learn an unconstrained transition map, the network is restricted to a model class built from known physical structure, so that its dynamics respect the physics by construction rather than only on average. In robotics, structure-preserving neural models have shown that such geometric priors improve data efficiency, extrapolation, and long-horizon stability [23]–[26]. Yet the strongest of these guarantees comes with a catch. Exact symplecticity holds only for closed conservative systems, while the systems we want to control are forced, dissipative, and contact-rich. As shown in Fig. 1, we resolve this by imposing symplecticity on the right space, embedding the physical state and its ports into a structured lifted space $T^*\mathcal{Q}$ where the learned map is exactly symplectic, while the projected physical dynamics it induces reside in $T^*\mathcal{Q}$ and may be constrained, forced or dissipative.

The practical stakes of this construction extend beyond prediction accuracy. Learned dynamics models are increasingly queried in closed loop, serving as the transition model inside model-predictive control and imagination-based policy optimization, where compounding rollout error is the binding constraint [19], [27]. This is where geometric fidelity earns its keep. A predictor that remains geometrically anchored over long horizons, while staying Markovian and requiring only a single forward pass, makes learned models usable inside such planners rather than merely alongside them.

The interface matches how modern robot controllers are actually built. The model predicts from the current state and ports alone, exactly the information a state-feedback controller or estimator holds at runtime, and the ports coincide with the joint torques and contact forces that predictive controllers already treat as decision variables [4]. A receding-horizon solver can query the lifted predictor directly, with no observation history to maintain and no context window to replay at every iteration. Robustness under distribution shift matters for the same reason. A deployed robot routinely meets terrains, payloads, and contact modes absent from training, and the out-of-distribution gains reported here target precisely this regime.

Our framework offers a second advantage beyond stability. Because the learned map is exactly symplectic and the ports enter as explicit canonical variables, the model exposes the energy exchange between robot and environment as a first-class quantity rather than an implicit byproduct of the fit. This opens a path toward passivity-based and certificate-based control

synthesis [28], [29], where energy bookkeeping is the object on which guarantees are built. Training stays equally practical, since teacher forcing avoids backpropagation through time and its attendant memory and gradient pathologies, keeping the model cheap to retrain as new operating data arrive. The predictor achieves all of this at parameter counts and inference costs compatible with control rates on embedded hardware.

A. Contributions

This work introduces CALISYM, a framework for learning Canonical Lifted Symplectic representations of real-world robot dynamics. The central idea is to enforce exact symplectic structure in a structured lifted phase space while allowing the induced physical dynamics to remain actuated, dissipative, and contact constrained. This bridges the gap between the theoretical guarantees of symplectic learning and the non-conservative dynamics encountered in practical robotic systems. Particularly, we make the following contributions:

- **Symplectic learning beyond conservative systems.** We introduce CALISYM, a framework that extends symplectic learning to controlled, dissipative, and constrained robotic systems (e.g. contacts).
- **Structured lift and gauge fixed rollout.** We introduce a structured lift that augments the physical state with variables governing energy exchange with the environment and constraints such as contacts. A gauge-fixed lift, projection, and re-embedding procedure enables autoregressive prediction under time varying controls and intermittent contacts. Due to the enforced symplectic priors the autoregressive error accumulation remains minimal, while the overall markovian rollouts remain stable.
- **GRB-SYMPNET.** We introduce GRB-SYMPNET, a generalized ridge B-spline symplectic architecture that combines local spline approximation with exactly symplectic flow layers, improving expressivity while preserving symplectic structure by construction. We further introduce a universal approximation theorem covering GRB-SYMPNET’s approximation capacity (see Appendix C).
- **Cross system evaluation.** We evaluate CALISYM on a simulated, forced and dissipative double pendulum, a **real-world** aerial quadrotor and a **real-world** contact-rich quadruped.

To the best of our knowledge, this is the first physics informed symplectic learning framework demonstrated across *real-world robotic systems* whose observed dynamics are controlled, dissipative, or contact constrained. The results show that the proposed framework is architecture agnostic, scales across system dimensions, and improves long-horizon autoregressive prediction while remaining parameter efficient.

II. RELATED WORK

CALISYM builds upon several developments spanning robot dynamics learning [30], geometric machine learning [31], and structure preserving representations of physical systems [32]. We review the works most closely related to the proposed framework and organize them according to the key design principles underlying our approach.

A. Learning Dynamics Models

Learning dynamics from data is a fundamental problem in robotics, underpinning model predictive control [4], state estimation [33], system identification [34], and model-based reinforcement learning [4], [5], [18]. Existing approaches span a broad spectrum of learning paradigms. At one end, black-box neural predictors and sequence models directly learn state transitions from data and have demonstrated strong empirical performance across a variety of robotic systems [35]–[37]. More recently, learned world models have extended this paradigm by constructing latent representations that jointly capture dynamics, observations, and control, enabling planning and imagination-based reinforcement learning [35], [36]. However, because these models are primarily black-box, they generally provide no guarantees regarding the preservation of physical quantities such as energy, momentum, or geometric structure, often leading to drift and instability during long-horizon rollouts [20].

A complementary direction is operator learning, where the objective is to learn mappings between function spaces rather than individual trajectories. Architectures such as Fourier Neural Operators (FNOs) [38], [39] and related neural operators have achieved remarkable success in modeling complex physical systems and partial differential equations by exploiting global spectral representations. While highly expressive, these methods are fundamentally designed to approximate solution operators and likewise do not explicitly enforce the geometric structure underlying mechanical systems. As a result, conservation laws and phase-space invariants may be violated even when short-term prediction accuracy is high, while their scalability is yet to be proven.

Within robotics, specialized sequence architectures such as RWM [40] augment autoregressive (AR) prediction with latent memory representations to improve long-horizon forecasting and capture history-dependent effects. By maintaining a learned latent state, these models can represent complex non-Markovian behaviors and partially mitigate error accumulation over extended prediction horizons. Nevertheless, the learned latent dynamics remain largely unconstrained by the underlying physical laws, providing no guarantees regarding the preservation of conservation laws, geometric structure, or physically meaningful invariants. As a result, predictions may become physically inconsistent under distribution shift or during long-horizon rollouts. Furthermore, training such recurrent and autoregressive world models typically relies on backpropagation through time (BPTT) [41], [42], requiring gradients to be propagated through long computational graphs. This introduces substantial memory and computational overhead while also exposing training to the well-known challenges of vanishing and exploding gradients, which can negatively impact optimization stability and scalability to increasingly long prediction horizons.

The common limitation across these families of methods is that physical structure is treated as an emergent property to be learned from data rather than a fundamental constraint imposed by the model architecture. In contrast, CALISYM incorporates a strong geometric inductive bias by constructing

the learned dynamics directly within a symplectic framework. This enables the model to preserve the underlying phase-space structure by design, substantially improving long-horizon stability, robustness to distribution shift, and the faithful reproduction of physically meaningful invariants. Its training relies entirely on teacher forcing, while the CALISYM’s predictions are entirely Markovian (i.e. single-step maps).

B. Geometric Models of Physical Systems

A complementary line of research seeks to improve generalization and long-horizon stability by embedding physical structure directly into the learning architecture rather than relying solely on data-driven regularization [21]. Hamiltonian Neural Networks (HNNs) learn a Hamiltonian function whose gradients generate the system dynamics [24], while Lagrangian Neural Networks (LNNs) parameterize the Lagrangian and recover the equations of motion through the Euler–Lagrange formalism [23]. These approaches leverage fundamental principles of classical mechanics to restrict the learned dynamics to physically plausible trajectories, resulting in improved extrapolation and data efficiency compared to unconstrained neural predictors.

A related but distinct class of methods focuses on preserving geometric structure directly at the level of the flow map. Symplectic neural networks such as SYMPNETs [26] construct discrete-time updates that preserve the canonical symplectic form exactly. By learning the dynamics map itself rather than an underlying energy function, these architectures avoid repeated differentiation during rollout and inherit the long-term stability properties associated with geometric numerical integrators. Consequently, they have emerged as one of the most promising directions for learning stable dynamics models from data, especially in data-scarce regimes.

Despite these advances, existing geometric learning methods remain largely confined to conservative mechanical systems. Real robotic platforms are fundamentally non-conservative, since they exchange energy with their environment through actuation, damping, friction, impacts, contacts, sensing, and control. As a result, the assumptions underlying the classical Hamiltonian formalism are frequently violated in practice. While HNNs and LNNs can incorporate certain extensions, they still require recovering the dynamics through differentiating learned energy functions, increasing computational cost and sensitivity to approximation errors. Existing symplectic architectures, on the other hand, preserve geometric structure exactly but are generally unable to represent dissipative or externally driven dynamics without sacrificing their underlying theoretical guarantees.

CALISYM bridges this gap by extending structure-preserving dynamics learning *beyond* conservative systems. Through a lifted symplectic representation, it retains the favorable stability and geometric properties of symplectic models while accommodating the strongly dissipative, actuated, and constrained dynamics encountered in real-world robotics. Moreover, the resulting predictor remains lightweight, parameter-efficient, and requires only a single forward pass per time step, making it practical for large-scale robotic learning and control applications.

C. Open and Constrained Dynamical Systems

Most real-world robotic systems are fundamentally non-conservative. Through actuation, damping, friction, impacts, contacts, and feedback control, they continuously exchange energy, momentum, and information with their environment. To model such phenomena, geometric mechanics has developed a variety of extensions to classical Hamiltonian theory, including port-Hamiltonian systems, dissipative and metriplectic dynamics, and controlled mechanical systems, which incorporate energy exchange and irreversible processes while preserving an underlying geometric structure [43]–[45]. Likewise, constrained Hamiltonian mechanics, presymplectic geometry, and Dirac structures provide principled frameworks for representing contacts, kinematic constraints, and admissible motions [46].

A recurring theme across these formulations is that apparently non-Hamiltonian behavior can often be represented as Hamiltonian dynamics on an appropriately augmented state space. Symplectification, cotangent lifts, and extended-phase-space constructions introduce auxiliary coordinates through which dissipation, forcing, and constraints arise as projections of a higher-dimensional conservative system [47], [48]. Despite their importance in geometric mechanics, these ideas have seen limited adoption in modern dynamics learning, where most symplectic architectures remain restricted to conservative systems. CALISYM builds directly on this geometric perspective, employing a lifted symplectic representation that enables the learning of dissipative, actuated, and constrained robotic dynamics while retaining the stability and structure-preserving properties of symplectic models.

D. Local Function Approximation

Recent advances in neural approximation theory have highlighted the benefits of localized function representations. Spline-based models and Kolmogorov–Arnold Networks (KANs) exploit the observation that many high-dimensional nonlinear mappings can be represented efficiently through compositions of low-dimensional functions, often yielding superior parameter efficiency and interpretability compared to conventional multilayer perceptrons [49], [50]. In particular, local basis functions are well suited to physical systems whose dynamics exhibit strongly nonlinear behavior only within restricted regions of the state space, a common characteristic of robotic systems with contacts, saturation effects, and configuration-dependent dynamics.

Despite their approximation power, generic spline and KAN-style architectures are purely function approximators and do not preserve the geometric structure of the underlying dynamical system. Consequently, improved local accuracy does not necessarily translate into physically consistent long-horizon predictions. For dynamical systems, preserving the structure of the flow can be as important as accurately approximating the vector field itself.

Our proposed GRB-SYMPNET combines the advantages of local function approximation with exact geometric preservation (see Appendix C). Building upon the generalized ridge formulation of SympNets, it replaces global nonlinearities with

compact tensor-product spline representations, enabling highly expressive local approximations of the scalar Hamiltonian while preserving symplecticity exactly by construction. The resulting architecture inherits the parameter efficiency and locality of spline-based models while retaining the long-term stability and geometric guarantees of structure-preserving symplectic networks.

III. ROBOT DYNAMICS AND HAMILTONIAN MECHANICS

Robot dynamics is primarily described by the Equations of Motion (EoMs) that connect the forces acting on the rigid bodies comprising the system and the accelerations they produce. There has been extensive research [3] on algorithms that efficiently assemble these EoMs, with most notable the Recursive Newton-Euler Algorithm (RNEA) and the Articulated-Body Algorithm (ABA) [51], [52]. However, they all rely on the rigid-body assumption, while phenomena such as friction are commonly modeled using the Lagrangian formalism.

A. Lagrangian Formalism

The Lagrangian formalism provides the variational counterpart to the Newton–Euler bookkeeping that RNEA and ABA carry out [53]. A robot’s configuration is a point on a smooth manifold rather than in a vector space, with the manifold determined by its kinematic structure. For a free-floating base together with n revolute joints, the base pose belongs to the special Euclidean group $\mathbb{SE}(3)$ and the joint angles to \mathbb{R}^n , so the configuration is the composite Lie group

$$\mathcal{Q} = \mathbb{SE}(3) \times \mathbb{R}^n, \quad (1)$$

a manifold of dimension $6 + n$. Each configuration $\mathbf{q} \in \mathcal{Q}$ carries velocities in its tangent space $T_{\mathbf{q}}\mathcal{Q}$, which the Lie-group structure identifies with the Lie algebra $\mathfrak{se}(3) \times \mathbb{R}^n \cong \mathbb{R}^{6+n}$. The generalized velocity \mathbf{v} pairs the base twist with the joint rates, the base component being an element of $\mathfrak{se}(3)$ rather than a derivative of pose coordinates. It relates to the configuration rate $\dot{\mathbf{q}} \in T_{\mathbf{q}}\mathcal{Q}$ through the tangent map of left translation,

$$\dot{\mathbf{q}} = \mathbf{q} \mathbf{v}^\wedge, \quad (2)$$

where $(\cdot)^\wedge$ maps the twist to its matrix form in $\mathfrak{se}(3)$ [54]. On the Euclidean factor this reduces to the identity $\dot{\mathbf{q}} = \mathbf{v}$, while on $\mathbb{SE}(3)$ it reconstructs the pose derivative from the body twist. The state (\mathbf{q}, \mathbf{v}) then lives in the tangent bundle $T\mathcal{Q}$.

On this bundle the Lagrangian is a map $L : T\mathcal{Q} \rightarrow \mathbb{R}$ given by kinetic minus potential energy,

$$L(\mathbf{q}, \mathbf{v}) := T(\mathbf{q}, \mathbf{v}) - V(\mathbf{q}), \quad (3)$$

where $T(\mathbf{q}, \mathbf{v})$ is the kinetic energy and $V(\mathbf{q})$ the potential energy. The Euler–Lagrange equations on \mathcal{Q} yield the canonical manipulator equation,

$$\mathbf{M}(\mathbf{q}) \dot{\mathbf{v}} + \mathbf{h}(\mathbf{q}, \mathbf{v}) + \mathbf{g}(\mathbf{q}) = \boldsymbol{\tau}, \quad (4)$$

with $\mathbf{M}(\mathbf{q})$ the joint-space inertia matrix, $\mathbf{h}(\mathbf{q}, \mathbf{v})$ the Coriolis and centrifugal terms, $\mathbf{g}(\mathbf{q})$ the gravitational generalized force, and $\boldsymbol{\tau}$ the applied generalized forces.

While the Lagrangian formulation on the tangent bundle $T\mathcal{Q}$ provides a familiar framework for deriving a robot’s equations of motion, its velocity-based state (\mathbf{q}, \mathbf{v}) carries three structural limitations. First, naive integration of the resulting vector field preserves none of the geometric invariants of the flow, so long-horizon simulations accumulate artificial energy drift and violate phase-space volume preservation. Second, symmetries and their associated conserved quantities remain implicit, rather than appearing as explicit geometric objects that integrators and learning models can exploit. Third, algebraic constraints from intermittent contact or closed kinematic loops are typically handled by penalty terms or Lagrange multipliers appended to the dynamics, an approach that degrades when the velocity-to-momentum map $\mathbf{p} = \mathbf{M}(\mathbf{q})\mathbf{v}$ becomes ill-conditioned under constraint projection and destabilizes the recursion.

B. Hamiltonian Formalism

Transitioning to the Hamiltonian formulation on the cotangent bundle $T^*\mathcal{Q}$, which pairs configurations with generalized momenta rather than velocities, resolves several limitations of the classical Lagrangian framework. The cotangent bundle is naturally equipped with the canonical symplectic two-form

$$\omega = \sum_{i=1}^n dq^i \wedge dp_i, \quad (5)$$

allowing the dynamics to be expressed as the first-order Hamiltonian system

$$\dot{\mathbf{q}} = \frac{\partial H}{\partial \mathbf{p}}, \quad \dot{\mathbf{p}} = -\frac{\partial H}{\partial \mathbf{q}}, \quad (6)$$

where H denotes the Hamiltonian of the system.

Beyond providing an equivalent description of the dynamics, this formulation exposes the geometric structure underlying mechanical systems. The Hamiltonian flow preserves the symplectic form exactly, and consequently preserves phase-space volume through Liouville’s theorem. When discretized using symplectic integrators, this structure often leads to favorable long-horizon numerical behavior and bounded energy drift. Furthermore, Noether’s theorem associates continuous symmetries with conserved momentum maps $\mathbf{J} : T^*\mathcal{Q} \rightarrow \mathfrak{g}^*$, exposing physically meaningful invariants such as linear and angular momentum. Finally, constrained Hamiltonian mechanics and the associated Dirac bracket formalism provide a principled mechanism for restricting trajectories to admissible constraint manifolds, making contacts and kinematic constraints part of the geometric structure of the system rather than external corrections.

These properties are particularly attractive from a learning perspective. By restricting the admissible dynamics to symplectic transformations on $T^*\mathcal{Q}$, the hypothesis space is dramatically reduced, providing a powerful geometric inductive bias that can improve data efficiency, extrapolation, and long-horizon stability.

C. Symplecticity in Machine Learning

Beyond their physical interpretation, these geometric properties fundamentally reshape the learning problem. By restricting the admissible dynamics to symplectomorphisms on $T^*\mathcal{Q}$, the model no longer needs to approximate arbitrary state transitions, but only those consistent with the underlying mechanics [55], [56]. This restriction acts as a strong inductive bias, reducing the effective hypothesis space and improving long horizon prediction, where unconstrained neural models often accumulate geometric errors that manifest as energy drift, instability, and violation of conserved quantities.

Since the Hamiltonian flow preserves the symplectic form exactly, satisfying $\mathcal{L}_{\mathbf{x}_H}\omega = 0$ [57], a data driven model can be constrained to learn a discrete time transition map Φ_θ satisfying $\Phi_\theta^*\omega = \omega$. Embedding this invariant directly into the network architecture yields learned dynamics that inherit the geometric structure of the underlying system, resulting in minimal long horizon energy error, volume preserving evolution, and improved autoregressive stability.

This perspective has motivated a broad class of Hamiltonian and symplectic neural networks. Their strongest theoretical guarantees, however, apply only when the observed state evolves as a closed conservative Hamiltonian system. Most robotic systems do not satisfy this assumption. A torque controlled double pendulum exchanges energy through actuation and damping. A quadrotor is driven by thrust and aerodynamic forces, while a legged robot exchanges energy and impulses through intermittent contact with the environment. Consequently, the measured physical state $\mathbf{x} := (\mathbf{q}, \mathbf{p})$ is generally forced, dissipative, and contact constrained. Imposing symplecticity directly on this state therefore enforces the wrong geometric structure.

D. Symplectic Learning beyond Conservative Systems

This paper proposes CALISYM. Rather than enforcing symplecticity on the measured physical state, we impose it on a structured lifted phase space that augments the state with variables governing energy exchange with the environment [48]. Dynamics are learned using exactly symplectic neural predictors in this lifted space and subsequently projected back to the physical state. Consequently, the learned model preserves symplectic structure in the lifted representation while remaining compatible with actuation, dissipation, and contact in the observed dynamics.

The lift is structured rather than latent. Given a physical state and port variables \mathbf{e} , such as control inputs or contact forces, the system is embedded into a gauge fixed section of a canonical lifted phase space. Prediction proceeds through lifting, symplectic evolution, projection, and re-embedding,

$$\mathbf{x}_k \xrightarrow{\sigma_{\mathbf{e}_k}} \mathbf{z}_k \xrightarrow{\Phi_\theta} \bar{\mathbf{z}}_{k+1} \xrightarrow{\Pi_{\mathcal{X}}} \hat{\mathbf{x}}_{k+1}. \quad (7)$$

For autoregressive rollout, the projected state is lifted again using the next port value,

$$\mathbf{z}_{k+1} = \sigma_{\mathbf{e}_{k+1}}(\hat{\mathbf{x}}_{k+1}). \quad (8)$$

This construction enables a single symplectic predictor to model systems with time varying controls, dissipation, and intermittent contact while preserving exact symplectic structure in the lifted space.

We also introduce **GRB-SYMPNET**, a generalized-ridge B-spline SympNet. GRB-SYMPNET keeps the exact symplectic generalized-ridge layer, but parameterizes the scalar ridge Hamiltonian with a compact B-spline/KAN-style local function. This improves local expressivity in low-dimensional lifted systems while preserving exact symplecticity. In this paper, GRB-SYMPNET is used for the controlled dissipative double pendulum. For the higher-dimensional quadrotor and quadruped experiments, we use GR-SYMPNET as the scalable lifted predictor. This separation is intentional: the structured lift is the transferable contribution across systems, while GRB-SYMPNET is an architecture contribution evaluated in the low-dimensional setting where spline ridge parameterizations are most appropriate.

We evaluate CALISYM on three systems of increasing complexity. The controlled dissipative double pendulum isolates the effect of the lift and tests whether GRB-SYMPNET improves low-dimensional lifted symplectic prediction. The quadrotor tests whether the same lifted formulation handles unbounded forced dynamics with time-varying controls. The quadruped tests whether the structured lift scales to high-dimensional contact-rich robot dynamics when paired with GR-SYMPNET. Together, these experiments test the main claim of the paper: symplectic robot learning can be extended beyond conservative systems by lifting the physical dynamics into a structured canonical phase space.

IV. METHODS

The goal of CALISYM is to learn a discrete time predictor for robotic systems whose measured physical dynamics are not closed Hamiltonian systems. The key idea is to separate where symplecticity is enforced from where prediction is evaluated. The measured state and its interaction variables are embedded into a structured canonical phase space, an exactly symplectic map is learned in that space, and the physical trajectory is recovered by projection. This section formalizes the lifted representation, states the geometric properties of the construction, describes the symplectic predictors used in our experiments, and gives the training, normalization, and verification procedures.

A. Problem Setting

Consider a robotic system evolving on a configuration manifold \mathcal{Q} with generalized coordinates $\mathbf{q} \in \mathcal{Q}$ and generalized momenta,

$$\mathbf{p} = \mathbf{M}(\mathbf{q})\mathbf{v}, \quad (9)$$

where $\mathbf{M}(\mathbf{q})$ denotes the generalized mass matrix and $\mathbf{v} \in T_{\mathbf{q}}\mathcal{Q}$ the generalized velocity. The measured physical state is therefore

$$\mathbf{x} = (\mathbf{q}, \mathbf{p}) \in T^*\mathcal{Q}. \quad (10)$$

Unlike closed Hamiltonian systems, robotic systems continuously exchange energy and momentum with their environment through actuation, dissipation, and contact. We represent these interactions through a collection of *physical ports*,

$$\mathbf{e} \in \mathcal{E}, \quad (11)$$

whose precise interpretation depends on the system under consideration. Examples include actuator torques, rotor thrusts, contact forces, or other externally supplied interaction variables.

A broad class of robotic systems with constraints such as contacts can be written as,

$$\begin{aligned} \mathbf{M}(\mathbf{q})\dot{\mathbf{v}} + \mathbf{h}(\mathbf{q}, \mathbf{v}) + \mathbf{g}(\mathbf{q}) + \mathbf{c}_{\text{diss}}(\mathbf{v}) &= \mathbf{B}(\mathbf{q})\mathbf{u} + \mathbf{J}_c(\mathbf{q})^\top \mathbf{f}_c \\ \text{s.t.: } \phi(\mathbf{q}) = 0, \text{ with } \mathbf{J}_c(\mathbf{q}) &= \frac{\partial \phi}{\partial \mathbf{q}}. \end{aligned} \quad (12)$$

The corresponding energy balance is

$$\frac{dH}{dt} = \mathbf{v}^\top \mathbf{B}(\mathbf{q})\mathbf{u} - \mathbf{v}^\top \mathbf{c}_{\text{diss}}(\mathbf{v}), \quad (13)$$

which shows that energy is continuously exchanged through actuation, and dissipative effects. Ideal contacts as constraints perform no work. Consequently, the measured state generally does not evolve as a closed conservative Hamiltonian system. The central challenge is therefore to retain the stability and geometric guarantees of symplectic learning while modeling dynamics that are inherently open. CALISYM addresses this challenge by constructing a lifted representation that admits an exactly symplectic formulation while remaining faithful to the underlying physical dynamics.

B. Structured Lift and Augmented Cotangent-lifted space

The central idea of CALISYM is to enforce symplecticity on an augmented canonical phase space rather than on the measured physical state itself. Let

$$\mathbf{x} = (\mathbf{q}, \mathbf{p}) \in \mathcal{X} := T^*\mathcal{Q} \quad (14)$$

denote the measured physical state, and let $\mathbf{e} \in \mathcal{E}$ denote the physical ports through which the system exchanges energy and momentum with its environment. Since the physical subsystem is generally open, the transition map on \mathcal{X} need not be symplectic. We therefore embed the physical state and ports into a structured lifted phase space on which an exactly symplectic map can be learned.

We define the lifted canonical state,

$$\mathbf{Z} = (\mathbf{Q}, \mathbf{P}) \in \mathcal{Z}, \quad \Omega = \sum_i dQ^i \wedge dP_i, \quad (15)$$

where Ω is the canonical symplectic form in the augmented space. For a controlled system with contact ports, we use:

$$\mathbf{Q} = (\mathbf{q}, \mathbf{y}, \boldsymbol{\lambda}_u, \boldsymbol{\lambda}_c), \quad (16)$$

$$\mathbf{P} = (\mathbf{r}, \mathbf{p}, \boldsymbol{\mu}_u, \boldsymbol{\pi}_c). \quad (17)$$

Here (\mathbf{q}, \mathbf{p}) are the physical configuration and momentum variables. The pair (\mathbf{r}, \mathbf{y}) consists of auxiliary conjugate fibers associated with the physical state. The pair $(\boldsymbol{\lambda}_u, \boldsymbol{\mu}_u)$ represents the actuation port, and $(\boldsymbol{\lambda}_c, \boldsymbol{\pi}_c)$ represents the contact port.

The lift is generic, hence blocks that are not present for a given system are omitted. With this ordering, the lifted symplectic form is

$$\Omega = d\mathbf{q} \wedge d\mathbf{r} + d\mathbf{y} \wedge d\mathbf{p} + d\boldsymbol{\lambda}_u \wedge d\boldsymbol{\mu}_u + d\boldsymbol{\lambda}_c \wedge d\boldsymbol{\pi}_c. \quad (18)$$

Here wedge products between vector-valued variables denote the corresponding componentwise sum. Equivalently, using a symplectic rotation transformation we define the equivalent base–fiber coordinates,

$$\mathbf{b} = (\mathbf{q}, \mathbf{p}, \boldsymbol{\mu}_u, \boldsymbol{\lambda}_c), \quad (19)$$

$$\boldsymbol{\zeta} = (\mathbf{r}, -\mathbf{y}, -\boldsymbol{\lambda}_u, \boldsymbol{\pi}_c). \quad (20)$$

Then the symplectic form becomes,

$$\Omega = \sum_i db^i \wedge d\zeta_i. \quad (21)$$

Thus, the lifted variables form a canonical cotangent representation over the base variables \mathbf{b} . The purpose of the lift is not merely to augment the state dimension, but to transform the learning problem into one of modeling Hamiltonian dynamics on an augmented canonical symplectic manifold. The lifted dynamics are generated by a Hamiltonian on this augmented phase space. Let

$$\mathbf{a}(\mathbf{q}, \mathbf{p}) \quad (22)$$

denote the physical configuration dynamics and let

$$\mathbf{f}(\mathbf{q}, \mathbf{p}, \boldsymbol{\mu}_u, \boldsymbol{\lambda}_c) \quad (23)$$

denote the corresponding momentum dynamics, including the effects of actuation, contact forces, and dissipation. Motivated by the cotangent lift of a forced vector field, we consider lifted Hamiltonians of the form,

$$\mathcal{H}_{\text{lift}}(\mathbf{b}, \boldsymbol{\zeta}) = \mathbf{r}^\top \mathbf{a}(\mathbf{q}, \mathbf{p}) - \mathbf{y}^\top \mathbf{f}(\mathbf{q}, \mathbf{p}, \boldsymbol{\mu}_u, \boldsymbol{\lambda}_c) + G(\mathbf{b}), \quad (24)$$

where G is an arbitrary scalar function of the base variables. The first term propagates the configuration dynamics, while the second couples the physical momentum evolution to the auxiliary fibers. The Hamiltonian is linear in the fiber variables (\mathbf{r}, \mathbf{y}) and therefore represents a cotangent lift of the physical dynamics augmented with canonical port variables.

C. Dynamics and Section Invariance

The lifted Hamiltonian induces a coupled evolution of the physical and auxiliary variables. The physical subsystem evolves according to:

$$\begin{aligned} \dot{\mathbf{q}} &= \mathbf{a}(\mathbf{q}, \mathbf{p}), & \dot{\mathbf{p}} &= \mathbf{f}(\mathbf{q}, \mathbf{p}, \boldsymbol{\mu}_u, \boldsymbol{\lambda}_c), \\ \dot{\mathbf{r}} &= -(\partial_{\mathbf{q}} \mathbf{a})^\top \mathbf{r} + (\partial_{\mathbf{q}} \mathbf{f})^\top \mathbf{y} - \nabla_{\mathbf{q}} G, \\ \dot{\mathbf{y}} &= (\partial_{\mathbf{p}} \mathbf{a})^\top \mathbf{r} - (\partial_{\mathbf{p}} \mathbf{f})^\top \mathbf{y} + \nabla_{\mathbf{p}} G, \\ \dot{\boldsymbol{\mu}}_u &= \mathbf{0}, & \dot{\boldsymbol{\lambda}}_u &= -(\partial_{\boldsymbol{\mu}_u} \mathbf{f})^\top \mathbf{y} + \nabla_{\boldsymbol{\mu}_u} G, \\ \dot{\boldsymbol{\lambda}}_c &= \mathbf{0}, & \dot{\boldsymbol{\pi}}_c &= (\partial_{\boldsymbol{\lambda}_c} \mathbf{f})^\top \mathbf{y} + \nabla_{\boldsymbol{\lambda}_c} G, \end{aligned} \quad (25)$$

The lifted dynamics evolve on the full augmented phase space \mathcal{Z} . In practice, however, only the physical state and interaction ports are observed. The measured data therefore occupy a distinguished gauge-fixed section of the lifted space

obtained by fixing the port variables and setting all auxiliary fibers to zero.

Under this gauge choice and given the ports,

$$\mathbf{e}_k = (\mathbf{u}_k, \mathbf{f}_{c,k}), \quad (26)$$

we define the physical data section,

$$\mathcal{S}_{\mathbf{e}_k} = \left\{ \mathbf{Z} \in \mathcal{Z} : \mathbf{r} = \mathbf{0}, \mathbf{y} = \mathbf{0}, \boldsymbol{\lambda}_u = \mathbf{0}, \boldsymbol{\pi}_c = \mathbf{0}, \boldsymbol{\mu}_u = \mathbf{u}_k, \boldsymbol{\lambda}_c = \mathbf{f}_{c,k} \right\}. \quad (27)$$

For systems without contacts, the contact block $(\boldsymbol{\lambda}_c, \boldsymbol{\pi}_c)$ is omitted. The corresponding section embedding

$$\sigma_{\mathbf{e}_k} : \mathcal{X} \rightarrow \mathcal{Z} \quad (28)$$

maps a measured state $\mathbf{x}_k = (\mathbf{q}_k, \mathbf{p}_k)$ onto $\mathcal{S}_{\mathbf{e}_k}$.

The physical section identifies the subset of lifted states that correspond to realizable observations. The physical coordinates and ports are preserved, while the auxiliary fibers vanish. Consequently, the physical dynamics are recovered by the projection $\Pi_{\mathcal{X}} : \mathcal{Z} \rightarrow \mathcal{X}$,

$$\Pi_{\mathcal{X}}(\mathbf{b}, \boldsymbol{\zeta}) = (\mathbf{q}, \mathbf{p}). \quad (29)$$

Although the physical section provides the initialization manifold for the observed data, it is not generally invariant under the lifted Hamiltonian dynamics. The auxiliary fibers may therefore evolve away from zero during prediction. This observation motivates the projection and re-embedding procedure introduced next, which restores consistency with the measured ports at every rollout step.

D. Autoregressive Gauge-Fixed Lifted Rollout

The gauge-fixed section identifies the subset of the augmented phase space corresponding to physically realizable observations. Since the lifted Hamiltonian flow is not generally constrained to remain on this section, prediction proceeds by alternating between the physical section and the full lifted phase space. At each step, the current physical state is embedded into the augmented space, evolved by an exactly symplectic map, projected back to the physical state, and subsequently re-embedded using the next port value.

A one-step prediction is computed as,

$$\begin{aligned} \mathbf{Z}_k &= \sigma_{\mathbf{e}_k}(\mathbf{x}_k), \\ \bar{\mathbf{Z}}_{k+1} &= \Phi_{\theta}^{\Delta t}(\mathbf{Z}_k), \\ \hat{\mathbf{x}}_{k+1} &= \Pi_{\mathcal{X}}(\bar{\mathbf{Z}}_{k+1}), \end{aligned} \quad (30)$$

where $\Phi_{\theta}^{\Delta t} : \mathcal{Z} \rightarrow \mathcal{Z}$ is exactly symplectic, i.e., $(\Phi_{\theta}^{\Delta t})^* \Omega = \Omega$. For autoregressive rollout, the projected physical prediction is re-embedded using the next measured or commanded port,

$$\mathbf{Z}_{k+1} = \sigma_{\mathbf{e}_{k+1}}(\hat{\mathbf{x}}_{k+1}). \quad (31)$$

Thus, the induced physical predictor is

$$\hat{\mathbf{x}}_{k+1} = \Pi_{\mathcal{X}} \circ \Phi_{\theta}^{\Delta t} \circ \sigma_{\mathbf{e}_k}(\mathbf{x}_k), \quad (32)$$

which need not be symplectic on the physical state alone.

This lift–evolve–project–re-embed procedure separates the learned symplectic dynamics from the physical mechanisms

Algorithm 1: Gauge-Fixed Lifted Rollout

Input: Initial state \mathbf{x}_0 , ports $\{e_k\}_{k=0}^H$, section embedding σ , projection $\Pi_{\mathcal{X}}$, symplectic predictor $\Phi_{\theta}^{\Delta t}$

Output: Predicted physical trajectory $\{\hat{\mathbf{x}}_k\}_{k=1}^H$

```

1  $\mathbf{Z}_0 \leftarrow \sigma_{e_0}(\mathbf{x}_0)$ ;
2 for  $k = 0, \dots, H - 1$  do
3    $\bar{\mathbf{Z}}_{k+1} \leftarrow \Phi_{\theta}^{\Delta t}(\mathbf{Z}_k)$ ;
4    $\hat{\mathbf{x}}_{k+1} \leftarrow \Pi_{\mathcal{X}}(\bar{\mathbf{Z}}_{k+1})$ ;
5    $\mathbf{Z}_{k+1} \leftarrow \sigma_{e_{k+1}}(\hat{\mathbf{x}}_{k+1})$ ;

```

responsible for energy exchange. The predictor evolves as an exactly symplectic map in the augmented phase space, while projection and re-embedding enforce consistency with the measured state and ports. Consequently, symplecticity is preserved in the lifted representation even though the induced dynamics on \mathcal{X} may be controlled, dissipative, and contact constrained.

E. Symplectic Predictors

The structured lift is architecture-agnostic, since any exactly symplectic map can be used as $\Phi_{\theta}^{\Delta t}$. In this paper, we use GR-SYMPNET for the quadrotor and quadraped experiments, and GRB-SYMPNET for the double pendulum. Both predictors are explicit discrete-time maps, so inference requires only a forward pass through the composed layers, not numerical integration of a learned vector field. Let

$$\mathbf{J}_{\Omega} = \begin{bmatrix} \mathbf{0} & \mathbf{I} \\ -\mathbf{I} & \mathbf{0} \end{bmatrix} \quad (33)$$

denote the canonical symplectic matrix. A differentiable map $\Phi : \mathcal{Z} \rightarrow \mathcal{Z}$ is symplectic when

$$D\Phi(\mathbf{Z})^{\top} \mathbf{J}_{\Omega} D\Phi(\mathbf{Z}) = \mathbf{J}_{\Omega}. \quad (34)$$

a) GR-SYMPNET: Let $(\mathbf{Q}, \mathbf{P}) \in \mathbb{R}^d \times \mathbb{R}^d$ denote lifted canonical coordinates. A GR-SYMPNET layer is generated by the scalar Hamiltonian

$$\mathcal{H}_{\ell}(\mathbf{Q}, \mathbf{P}) = K_{\ell}(\boldsymbol{\xi}_{\ell}), \text{ where } \boldsymbol{\xi}_{\ell} = \mathbf{A}_{\ell}\mathbf{P} + \mathbf{B}_{\ell}\mathbf{Q}, \quad (35)$$

and

$$\mathbf{A}_{\ell}, \mathbf{B}_{\ell} \in \mathbb{R}^{m \times d} \text{ with } m \ll d. \quad (36)$$

Furthermore, symplecticity is preserved *iff*

$$\mathbf{A}_{\ell}\mathbf{B}_{\ell}^{\top} = \mathbf{B}_{\ell}\mathbf{A}_{\ell}^{\top}. \quad (37)$$

Hamilton's equations for (35) give

$$\dot{\mathbf{Q}} = \mathbf{A}_{\ell}^{\top} \nabla K_{\ell}(\boldsymbol{\xi}_{\ell}), \quad (38)$$

$$\dot{\mathbf{P}} = -\mathbf{B}_{\ell}^{\top} \nabla K_{\ell}(\boldsymbol{\xi}_{\ell}). \quad (39)$$

The ridge coordinate is invariant along the layer flow:

$$\dot{\boldsymbol{\xi}}_{\ell} = \mathbf{A}_{\ell}\dot{\mathbf{P}} + \mathbf{B}_{\ell}\dot{\mathbf{Q}} \quad (40)$$

$$= (-\mathbf{A}_{\ell}\mathbf{B}_{\ell}^{\top} + \mathbf{B}_{\ell}\mathbf{A}_{\ell}^{\top}) \nabla K_{\ell}(\boldsymbol{\xi}_{\ell}) \quad (41)$$

$$= \mathbf{0}. \quad (42)$$

Therefore, the exact time- h_{ℓ} map is

$$\mathbf{Q}' = \mathbf{Q} + h_{\ell}\mathbf{A}_{\ell}^{\top} \nabla K_{\ell}(\boldsymbol{\xi}_{\ell}), \quad (43)$$

$$\mathbf{P}' = \mathbf{P} - h_{\ell}\mathbf{B}_{\ell}^{\top} \nabla K_{\ell}(\boldsymbol{\xi}_{\ell}). \quad (44)$$

Each layer is an exact Hamiltonian flow and is therefore symplectic. The full predictor is a composition

$$\Phi_{\theta}^{\Delta t} = \phi_L \circ \dots \circ \phi_1, \quad (45)$$

and remains symplectic by closure of symplectic maps under composition. Since $\boldsymbol{\xi}_{\ell} \in \mathbb{R}^m$ with $m \ll d$, the nonlinear computation is performed in a low-dimensional ridge coordinate, which keeps the high-dimensional quadraped predictor parameter-efficient.

b) GRB-SYMPNET: GRB-SYMPNET keeps the exact generalized-ridge symplectic layer in (44), but changes the scalar function K_{ℓ} . We write:

$$K_{\ell}(\boldsymbol{\xi}) = K_{\ell, \text{spline}}(\boldsymbol{\xi}) + K_{\ell, \text{smooth}}(\boldsymbol{\xi}). \quad (46)$$

The spline term is

$$K_{\ell, \text{spline}}(\boldsymbol{\xi}) = \sum_{\alpha \in \mathcal{A}} c_{\ell, \alpha} \prod_{j=1}^m B_{\alpha_j}^{(r)}(\xi_j), \quad (47)$$

where $B_{\alpha_j}^{(r)}$ is a degree- r B-spline basis function. The smooth term provides a bounded global tail:

$$K_{\ell, \text{smooth}}(\boldsymbol{\xi}) = \sum_{j=1}^{N_s} a_{\ell j} \varphi(\mathbf{w}_{\ell j}^{\top} \boldsymbol{\xi} + b_{\ell j}). \quad (48)$$

Because K_{ℓ} appears only as a scalar Hamiltonian in the exact generalized-ridge layer, replacing it with a spline parameterization does not affect symplecticity. The spline is evaluated in the low-dimensional ridge coordinate $\boldsymbol{\xi} \in \mathbb{R}^m$, not in the full lifted state. This gives a local KAN-style approximation while preserving the explicit low-latency symplectic map. GRB-SYMPNETs proved to be parameter efficient but they inherit the same limitation with KAN-based architectures in terms of scalability. Hence, we use them only for the double-pendulum experiments. Finally, similar to (44) the required gradients are calculated analytically, so no additional backward pass is required.

F. Training, Normalization, and Verification

The datasets provide configurations and generalized velocities. We convert velocities to momenta using

$$\mathbf{p}_k = \mathbf{M}(\mathbf{q}_k) \mathbf{v}_k. \quad (49)$$

For the double pendulum and quadrotor, $\mathbf{M}(\mathbf{q})$ is computed from the analytical model. For the quadraped, $\mathbf{M}(\mathbf{q})$ is computed from the robot model. For systems with Lie-group configuration components, errors are computed in local coordinates. We write

$$\mathbf{q}_1 \ominus \mathbf{q}_2 \in T_{\mathbf{q}_2} \mathcal{Q} \quad (50)$$

for the local configuration difference. For Euclidean joints this is ordinary subtraction. For orientation components, it is computed using the logarithm map. The physical state error is

$$\mathbf{x}_1 \ominus \mathbf{x}_2 = (\mathbf{q}_1 \ominus \mathbf{q}_2, \mathbf{p}_1 - \mathbf{p}_2). \quad (51)$$

Hence, the one-step loss is

$$\mathcal{L}_1 = \frac{1}{|\mathcal{D}|} \sum_k \|\mathbf{W}_x (\Pi_{\mathcal{X}} [\Phi_{\theta}^{\Delta t}(\sigma_{e_k}(\mathbf{x}_k))] \ominus \mathbf{x}_{k+1})\|_2^2, \quad (52)$$

where \mathbf{W}_x balances configuration and momentum errors. For multi-step training over horizon H , we roll out with Algorithm 1 and minimize the Teacher-Forcing (TF) loss:

$$\mathcal{L}_H = \frac{1}{H} \sum_{j=0}^{H-1} \|\mathbf{W}_x (\hat{\mathbf{x}}_{j+1} \ominus \mathbf{x}_{j+1})\|_2^2. \quad (53)$$

We also penalize drift away from the data section before re-embedding. If

$$\bar{\mathbf{Z}}_{j+1} = (\bar{\mathbf{b}}_{j+1}, \bar{\boldsymbol{\zeta}}_{j+1}) \quad (54)$$

is the lifted prediction before gauge fixing, then

$$\mathcal{L}_{\text{sec}} = \frac{1}{H} \sum_{j=0}^{H-1} \|\mathbf{W}_{\zeta} \bar{\boldsymbol{\zeta}}_{j+1}\|_2^2. \quad (55)$$

This term encourages the learned map to remain close to the measured data section over one step. It does not enforce symplecticity, since symplecticity is structurally enforced by the predictor architecture. The total objective is:

$$\mathcal{L} = w_1 \mathcal{L}_1 + w_H \mathcal{L}_H + w_{\text{sec}} \mathcal{L}_{\text{sec}} + w_{\text{reg}} \|\theta\|_2^2. \quad (56)$$

The lifted variables have heterogeneous units and scales. We therefore normalize in base-fiber coordinates. For each pair (b_i, ζ_i) , define

$$\tilde{b}^i = \frac{b^i - \mu^i}{s^i}, \quad \tilde{\zeta}_i = s_i \zeta_i. \quad (57)$$

Then

$$d\tilde{b}^i \wedge d\tilde{\zeta}_i = db^i \wedge d\zeta_i, \quad (58)$$

so the normalization preserves the canonical symplectic form. This is essential, since independently standardizing all entries of $(\mathbf{b}, \boldsymbol{\zeta})$ would generally destroy the canonical pairing.

Finally, although GR-SYMPNET and GRB-SYMPNET are symplectic by construction, we verify this numerically through the Jacobian residual

$$\epsilon_{\mathbf{J}_{\Omega}} = \frac{\|D\Phi_{\theta}^{\Delta t}(\mathbf{Z})^{\top} \mathbf{J}_{\Omega} D\Phi_{\theta}^{\Delta t}(\mathbf{Z}) - \mathbf{J}_{\Omega}\|_F}{\|\mathbf{J}_{\Omega}\|_F}. \quad (59)$$

For exactly symplectic predictors, this residual should be at numerical precision. For unconstrained baselines, it is not expected to vanish. At inference time, the model is rolled out autoregressively using Algorithm 1. Each step amounts to a lift, one explicit symplectic forward pass, a projection, and a re-embedding with the next port value.

V. RESULTS

We evaluate CALISYM on robotic systems whose observed dynamics violate the assumptions underlying classical symplectic learning. In particular, we consider controlled, dissipative, and contact-rich systems, where the measured physical dynamics do not evolve as closed conservative Hamiltonian systems. The objective of these experiments is to determine whether enforcing symplectic structure in a structured lifted

phase space improves long-horizon prediction while remaining applicable across systems of different dimensionality and complexity.

Our evaluation is designed to answer the following questions:

- 1) Can symplectic learning be extended beyond conservative systems by enforcing symplectic structure in a structured lifted phase space?
- 2) Does the proposed lifted formulation improve markovian long-horizon autoregressive prediction while remaining parameter-efficient?
- 3) Does the same lift construction transfer across robotic systems with substantially different dimensionality and interaction mechanisms, ranging from controlled dissipative systems to contact-rich locomotion?

To investigate these questions, we consider three representative systems of increasing complexity. A controlled dissipative double pendulum serves as a low-dimensional benchmark for isolating the effect of the proposed lift and evaluating GRB-SYMPNET in the chaotic regime [58]. A real-world quadrotor platform introduces floating-base, nonlinear dynamics, testing whether the framework extends beyond simple mechanical systems. Finally, the real-world quadrupedal dynamics of ANYmal D [59] involving floating-base motion, underactuation, and intermittent contact provides a demanding high-dimensional benchmark for evaluating scalability when combined with GR-SYMPNET. Together, these experiments assess the effectiveness of the proposed lifted symplectic representation across dissipative, controlled, and contact-rich robotic systems, as well as its impact on long-horizon autoregressive prediction accuracy.

A. Baselines and Metrics

All models are trained using one-step teacher forcing and evaluated under autoregressive rollout. We deliberately avoid autoregressive training objectives to isolate the quality of the learned dynamics representation from the effects of the training procedure. While autoregressive training can improve rollout performance by exposing models to their own prediction errors, it may also encourage compensation for rollout-induced distribution shift and introduce additional optimization challenges for long prediction horizons [60], [61]. Teacher forcing therefore provides a cleaner comparison of each architecture’s ability to learn the underlying dynamics.

Importantly, all OOD evaluations are performed on trajectories drawn from previously unseen dynamical regimes, rather than on held-out segments of trajectories observed during training. The OOD splits correspond to distinct energy regimes for the double pendulum, held-out flight trajectories for the quadrotor, and unseen locomotion scenarios and environments for the quadruped. This contrasts with common evaluation protocols in the physics informed literature that train on partial trajectories and evaluate on disjoint temporal segments of the same underlying trajectories [62], [63].

We compare CALISYM against both black-box and physics-informed baselines, including an MLP, a Transformer, teacher-forcing-trained RWM-TF [40], a Dissipative Hamiltonian Neu-

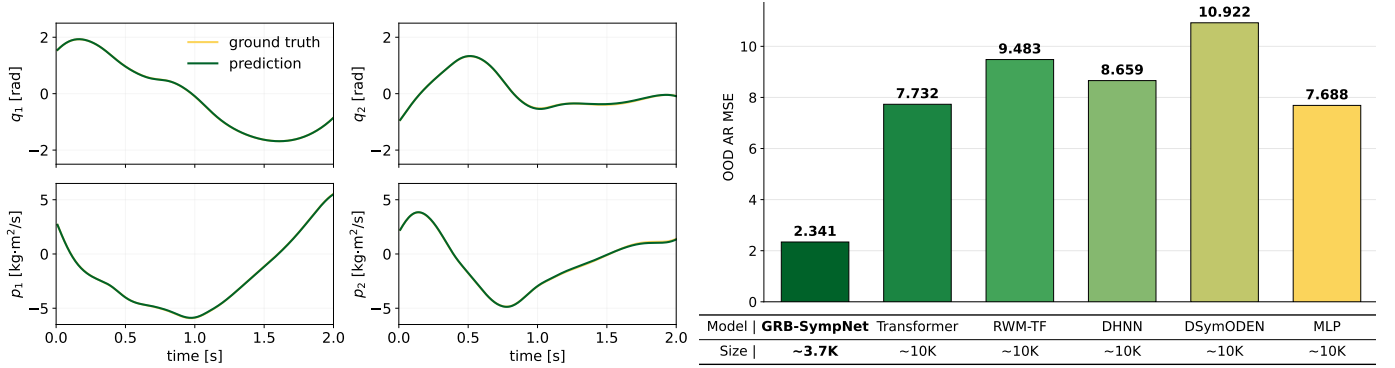


Fig. 2. **Controlled dissipative double pendulum.** A simulated torque-controlled, damped system. **(Left)** An autoregressive out-of-distribution 200-timestep rollout of the physical state (q_1, q_2, p_1, p_2) , the joint angles and their corresponding momenta. **(Right)** The bar plot reports out-of-distribution autoregressive MSE and model size. CALISYM with GRB-SYMPNET achieves the lowest OOD error (2.341 vs. 7.688 for the strongest baseline, a $\sim 69.5\%$ reduction) using only $\sim 3.7\text{K}$ parameters against $\sim 10\text{K}$ for the baselines, showing the gain comes from structure rather than capacity.

ral Network (DHNN) [24], and Dissipative SymODEN (D-SymODEN) [64]. The Transformer and RWM-TF operate on a 32-step context window and therefore receive access to multiple past observations, whereas all other methods, including CALISYM, predict using only the current state and port variables.

Unless otherwise stated, CALISYM is instantiated using either GRB-SYMPNET or GR-SYMPNET depending on the dimensionality of the lifted state space. All results are reported under autoregressive rollout, the regime most relevant to planning and model-predictive control. We report out-of-distribution autoregressive mean-squared error (OOD AR MSE) and parameter count, thereby evaluating both long-horizon predictive accuracy and model efficiency.

B. Controlled Dissipative Double Pendulum

We first evaluate CALISYM on a controlled dissipative double pendulum, a benchmark that isolates the central challenge addressed by this work, i.e., learning non-conservative, complex dynamics using a symplectic lifted representation. The system consists of two coupled rotational degrees of freedom subject to gravity, viscous damping, and external torque inputs as shown in Table I. Although the underlying mechanical dynamics originate from a Hamiltonian system, damping and control inputs continuously inject and dissipate energy, making the observed dynamics fundamentally non-conservative.

TABLE I
DOUBLE PENDULUM PHYSICAL PARAMETERS.

Parameter	Value
(m_1, m_2) [kg]	(2.1, 1.3)
(l_1, l_2) [m]	(0.4, 1.3)
(I_1, I_2) [$\text{kg} \cdot \text{m}^2$]	(1.1, 0.7)
(k_1, k_2) [$\text{N} \cdot \text{m}/\text{rad}$]	(0.03, 0.06)
(b_1, b_2) [$\text{N} \cdot \text{m} \cdot \text{s}/\text{rad}$]	(0.3, 0.6)
g [m/s^2]	9.81

The measured state is

$$\mathbf{x} = (\mathbf{q}, \mathbf{p}) \in \mathbb{R}^4, \quad (60)$$

where $\mathbf{q} = (q_1, q_2)$ denotes the joint angles and $\mathbf{p} = (p_1, p_2)$ the corresponding generalized momenta. The physical state and control torques are embedded into the lifted section

$$\mathbf{Q} = (\mathbf{q}, \mathbf{0}, \mathbf{0}) \in \mathbb{R}^6, \quad \mathbf{P} = (\mathbf{0}, \mathbf{p}, \boldsymbol{\tau}) \in \mathbb{R}^6, \quad (61)$$

and evolved using GRB-SYMPNET within the lifted symplectic phase space. Figure 2 shows representative autoregressive rollouts together with a quantitative comparison against all baselines. CALISYM accurately tracks both joint angles and generalized momenta over long prediction horizons despite the presence of actuation and dissipation. Quantitatively, CALISYM achieves an OOD AR MSE of 2.341, compared to 7.688 for the strongest competing baseline, corresponding to a 69.5% reduction in rollout error. This improvement is obtained using only approximately 3.7K parameters, whereas competing methods require roughly 10K parameters. The results suggest that the lifted symplectic representation successfully resolves the mismatch between non-conservative physical dynamics and conventional symplectic learning, while the local spline approximation of GRB-SYMPNET provides sufficient expressivity to capture the resulting dynamics with a compact model.

C. Quadrotor Dynamics

The quadrotor experiment evaluates whether the proposed structured lift remains effective for underactuated aerial systems with strongly control-dependent dynamics. Unlike the quadruped, where energy and momentum are exchanged through both actuation and intermittent contact, the quadrotor interacts with its environment primarily through rotor thrust and aerodynamic effects. Rotor inputs continuously inject energy into the system, while aerodynamic drag and other unmodeled effects introduce dissipation that is difficult to capture through purely conservative formulations. The used real-world dataset [65], [66] comprises 54 flights of a quadrotor with parameters as shown in II.

The physical state consists of the vehicle pose, orientation, and generalized momenta. The available ports correspond to the commanded rotor thrusts and body torques. CALISYM embeds the physical state together with the control ports into the lifted section,

$$\mathbf{Q} = (\mathbf{q}, \mathbf{0}, \mathbf{0}) \in \mathbb{R}^{18}, \quad \mathbf{P} = (\mathbf{0}, \mathbf{p}, \boldsymbol{\tau}) \in \mathbb{R}^{18}, \quad (62)$$

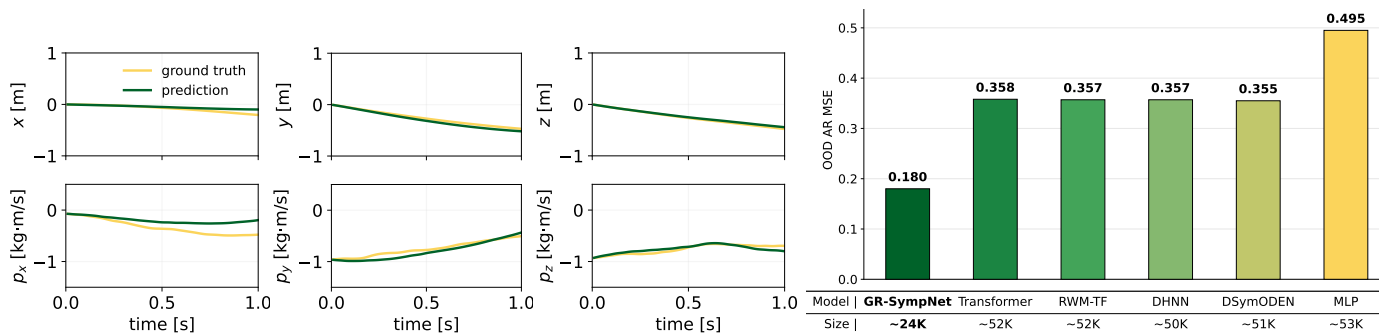


Fig. 3. **Quadrotor dynamics.** An underactuated aerial forced system with rotor thrust, aerodynamic and other unmodeled effects. **(Left)** An autoregressive 100-timestep out-of-distribution rollout of the body position (x, y, z) and corresponding momenta. **(Right)** The bar plot reports out-of-distribution autoregressive MSE and model size. CALISYM achieves the lowest OOD rollout error while remaining parameter-efficient, showing that the same lift transfers without modification to forced aerial dynamics.

TABLE II
QUADROTOR (ASCTEC PELICAN) PHYSICAL PARAMETERS.

Parameter	Value
m [kg]	1.6
(I_{xx}, I_{yy}, I_{zz}) [kg m ²]	(0.002, 0.002, 0.001)
k_f	9.9865×10^{-6}
k_m	1.5978×10^{-7}
l [m]	0.21

where τ denotes the control inputs. The lifted dynamics are evolved using an exactly symplectic GR-SYMPNET predictor before being projected back onto the physical state space through the gauge-fixed rollout procedure described in Section IV.

This experiment is particularly challenging because quadrotor dynamics are highly sensitive to control inputs and rapidly accumulate prediction errors during autoregressive rollout. Small inaccuracies in attitude prediction can quickly propagate into translational motion, resulting in substantial trajectory drift. Consequently, the task provides a stringent test of whether the proposed lifted representation can maintain stable long-horizon predictions despite the strongly forced and dissipative nature of the underlying dynamics.

Figure 3 shows representative autoregressive rollouts together with the corresponding OOD comparison. CALISYM achieves the lowest OOD rollout error among the evaluated methods while remaining parameter-efficient. More importantly, the results demonstrate that the same lift formulation used for the double pendulum transfers directly to aerial dynamics without modification, supporting the claim that the structured lift is a general mechanism for extending symplectic learning beyond conservative systems.

D. Quadruped Dynamics

The quadruped experiment evaluates whether the proposed lifted symplectic representation remains effective in the high-dimensional, contact-rich regime characteristic of real robotic systems. The physical state comprises floating-base and joint coordinates together with their corresponding generalized momenta [67]. We evaluate CALISYM on the GRANDTOUR locomotion dataset [68], which contains extensive real-world tra-

jectories of a quadruped robot performing diverse locomotion behaviors across varying commands, terrains, and environmental conditions. This benchmark poses a particularly challenging dynamics-learning problem due to the combination of floating-base motion, intermittent contacts, impacts, actuator dynamics, contact slippage, and rapidly changing contact modes, all of which can amplify small modeling errors during long-horizon autoregressive rollout.

CALISYM represents these effects by embedding control torques and contact forces into the lifted section

$$\mathbf{Q} = (\mathbf{q}, \mathbf{0}, \mathbf{0}, \mathbf{f}_c) \in \mathbb{R}^{66}, \quad \mathbf{P} = (\mathbf{0}, \mathbf{p}, \bar{\boldsymbol{\tau}}, \mathbf{0}) \in \mathbb{R}^{66}, \quad (63)$$

where $\bar{\boldsymbol{\tau}} = (\mathbf{0}_6, \boldsymbol{\tau})$ augments the joint torques with zeros corresponding to the unactuated floating-base coordinates. The lifted dynamics are modeled using GR-SYMPNET, whose generalized-ridge parameterization scales efficiently to the resulting high-dimensional state space.

Figure 4 presents representative autoregressive rollouts together with an OOD comparison against all baselines. The rollout trajectories demonstrate that CALISYM accurately captures both the dominant floating-base motion and the evolution of representative leg joints despite the heterogeneous scales of base coordinates, joint angles, contact forces, and generalized momenta. Quantitatively, CALISYM achieves the lowest OOD autoregressive error among all evaluated methods, obtaining an OOD AR MSE of 2.697 compared to 3.089 for the Transformer, 3.565 for RWM-TF, 4.676 for DHNN, and 5.080 for D-SymODEN. This corresponds to a 12.7% reduction relative to the strongest baseline and a 46.9% reduction relative to D-SymODEN.

Importantly, these improvements are achieved with smaller network sizes compared to the baselines. CALISYM uses approximately 316K parameters, compared to roughly 400K parameters for the Transformer, DHNN, and D-SymODEN, and approximately 720K parameters for RWM-TF. The results therefore suggest that the gains arise from the lifted symplectic representation and the associated symplectic inductive bias rather than large model size. Moreover, they demonstrate that the generalized-ridge architecture of GR-SYMPNET can scale the proposed framework to realistic contact-rich robotic systems without resorting to large autoregressive sequence models with large context windows.

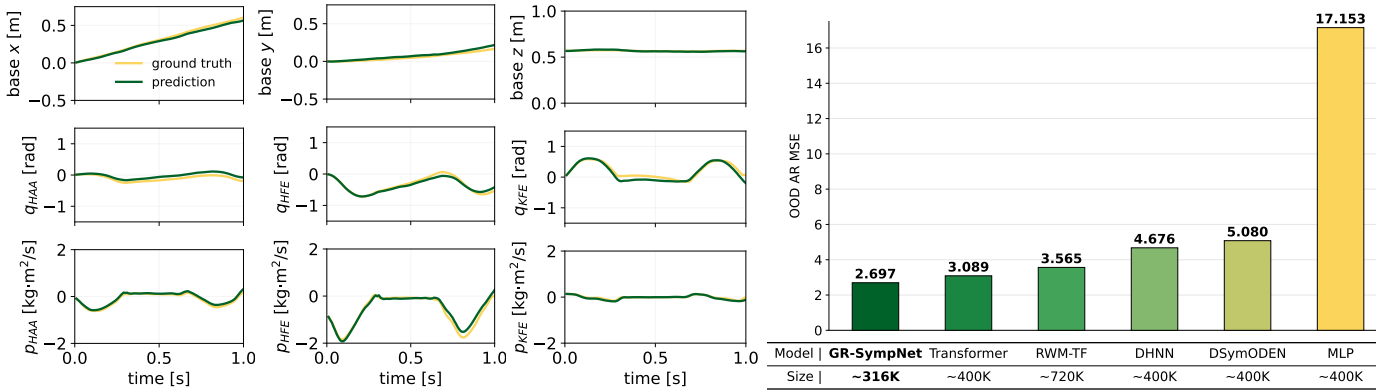


Fig. 4. **Quadruped dynamics.** A high-dimensional, contact-rich floating-base system actuated through joint torques and ground contact. **(Left)** An autoregressive out-of-distribution rollout of the floating-base position and representative right-leg coordinates and momenta, where q_{HAA} , q_{HFE} , q_{KFE} denote hip abduction/adduction, hip flexion/extension, and knee flexion/extension, with conjugate momenta p_{HAA} , p_{HFE} , p_{KFE} . CALISYM embeds joint torques and contact forces into the lift, keeping the projected dynamics contact-rich and non-conservative. **(Right)** The bar plot reports out-of-distribution autoregressive MSE and model size. CALISYM with GR-SYMPNET achieves the lowest OOD error (2.697 vs. 3.089 for the strongest baseline, a $\sim 12.7\%$ reduction) with $\sim 316K$ parameters, fewer than the main baselines (400K–720K).

E. Summary

Across the double pendulum, quadrotor, and quadruped benchmarks, the results consistently support the central hypotheses of this work. First, learning dynamics in a structured lifted symplectic space improves long-horizon prediction for non-conservative systems. Despite actuation, dissipation, and contact interactions, CALISYM achieves the lowest OOD autoregressive rollout error across all three systems.

Second, these improvements come with strictly smaller models. CALISYM uses roughly $3.7K$ parameters against $10K$ for every baseline on the double pendulum, $24K$ against $\sim 50K$ on the quadrotor, and $316K$ against $400K$ to $720K$ on the quadruped, ruling out capacity as the main source of the gains. The comparison is if anything conservative, since the Transformer and RWM-TF additionally condition on a 32-step context window while CALISYM predicts from the current state and ports alone (fully markovian rollout). That both GRB-SYMPNET and GR-SYMPNET outperform these larger baselines at every scale indicates the gains arise from the geometric inductive bias of the lifted representation, not from capacity or access to history.

Third, the same lift-evolve-project-re-embed procedure transfers across systems with substantially different dimensionality and interaction mechanisms, from a controlled dissipative pendulum to an aerial quadrotor and an underactuated quadruped. Empirically, parameter count scales quadratically with the lifted phase-space dimension (d) across the three systems, consistent with $\Theta(md)$ ridge matrices whose width m is chosen proportional to d . Fixing the ridge dimension instead would recover linear scaling, at the cost of per-layer expressivity.

Taken together, these results demonstrate that symplectic dynamics learning is not confined to conservative Hamiltonian systems. The lift is what makes this possible. Evolution in the lifted phase space remains symplectic by construction, so the geometric prior responsible for stability is preserved regardless of what happens physically, and control, dissipation, and constraint enter only through the projection back to the

physical state. By enforcing symplectic structure in this lifted space while leaving the induced physical dynamics free to be controlled, dissipative, or constrained, CALISYM unites the stability of geometric learning with the flexibility that real-world robotics demands.

VI. CONCLUSION

We introduced CALISYM, a framework for learning symplectic representations of robotic systems whose observed dynamics are controlled, dissipative, and constrained. The central idea is to enforce symplectic structure in a structured lifted canonical phase space rather than directly on the measured physical state, allowing the induced physical dynamics to remain non-conservative.

The proposed framework separates geometric structure from physical energy exchange. Dynamics are learned as exact symplectic maps in the lifted space, while projection and re-embedding ensure consistency with the observed state, controls, and constraints. Because the ports enter as explicit canonical variables, this separation also exposes the energy exchange between the robot and its environment as a first-class quantity rather than an implicit byproduct of the fit, opening a path from learned dynamics toward passivity-based and certificate-based control synthesis [28], [69]. The model predicts from the current state and ports alone, which is the information a receding-horizon solver already holds at each step of its internal rollout, so there is no observation history to maintain and no context window to replay at every iteration. This construction retains the computational advantages of explicit SympNet-style predictors while extending their applicability beyond closed Hamiltonian systems.

Across controlled dissipative and contact-constrained robotic systems, CALISYM consistently improves out-of-distribution autoregressive prediction while remaining parameter-efficient. The predictor achieves this at parameter counts and inference costs compatible with control rates on embedded hardware, making the underlying guarantees practically realizable rather than a purely theoretical consideration.

These results demonstrate that symplectic learning can be extended beyond conservative systems through a structured canonical lift, providing a practical geometric inductive bias for long-horizon robot dynamics prediction.

Future work will investigate richer port representations, uncertainty-aware lifted dynamics, and integration with model-predictive control, trajectory optimization, and planning pipelines. More generally, this work suggests that physically meaningful geometric structure can be recovered and exploited even when it is not apparent in the measured dynamics, opening new opportunities for structure-preserving learning in complex robotic systems.

REFERENCES

- [1] J. H. Connell and S. Mahadevan, *Robot learning*. Springer Science & Business Media, 2012, vol. 233.
- [2] R. M. Murray, Z. Li, and S. S. Sastry, *A mathematical introduction to robotic manipulation*. CRC press, 2017.
- [3] R. Featherstone, *Rigid Body Dynamics Algorithms*, ser. Engineering. Springer US, 2014.
- [4] C. Mastalli, W. Merkt, G. Xin, J. Shim, M. Mistry, I. Havoutis, and S. Vijayakumar, “Agile maneuvers in legged robots: a predictive control approach,” 2022. [Online]. Available: <https://arxiv.org/abs/2203.07554>
- [5] T. D. Barfoot, *State estimation for robotics*. Cambridge University Press, 2024.
- [6] H. Dai, A. Valenzuela, and R. Tedrake, “Whole-body motion planning with centroidal dynamics and full kinematics,” in *2014 IEEE-RAS International Conference on Humanoid Robots*, 2014, pp. 295–302.
- [7] A. Papatheodorou, W. Merkt, A. L. Mitchell, and I. Havoutis, “Momentum-aware trajectory optimisation using full-centroidal dynamics and implicit inverse kinematics,” in *2024 IEEE/RSJ International Conference on Intelligent Robots and Systems (IROS)*, 2024, pp. 11 940–11 947.
- [8] P.-B. Wieber, *Holonomy and Nonholonomy in the Dynamics of Articulated Motion*. Springer Berlin Heidelberg, 2006, pp. 411–425.
- [9] O. G. Selfridge, R. S. Sutton, and A. G. Barto, “Training and tracking in robotics,” in *Ijcai*, 1985, pp. 670–672.
- [10] H. Nguyen, M. Kamel, K. Alexis, and R. Siegwart, “Model predictive control for micro aerial vehicles: A survey,” in *2021 European Control Conference (ECC)*, 2021, pp. 1556–1563.
- [11] R. Tedrake, *Underactuated Robotics*, 2023. [Online]. Available: <https://underactuated.csail.mit.edu>
- [12] B. Ai, S. Tian, H. Shi, Y. Wang, T. Pfaff, C. Tan, H. I. Christensen, H. Su, J. Wu, and Y. Li, “A review of learning-based dynamics models for robotic manipulation,” *Science Robotics*, vol. 10, no. 106, p. eadt1497, 2025. [Online]. Available: <https://www.science.org/doi/abs/10.1126/scirobotics.adt1497>
- [13] T. Tsuji, Y. Kato, G. Solak, H. Zhang, T. Petrić, F. Nori, and A. Ajoudani, “A survey on imitation learning for contact-rich tasks in robotics,” 2025. [Online]. Available: <https://arxiv.org/abs/2506.13498>
- [14] S. Ha, J. Lee, M. van de Panne, Z. Xie, W. Yu, and M. Khadiv, “Learning-based legged locomotion: State of the art and future perspectives,” *Int. J. Rob. Res.*, vol. 44, no. 8, p. 1396–1427, Jul. 2025. [Online]. Available: <https://doi.org/10.1177/02783649241312698>
- [15] J. Liu, P. Borja, and C. Della Santina, “Physics-informed neural networks to model and control robots: A theoretical and experimental investigation,” *Advanced Intelligent Systems*, vol. 6, no. 5, p. 2300385, 2024. [Online]. Available: <https://advanced.onlinelibrary.wiley.com/doi/abs/10.1002/aisy.202300385>
- [16] D. Ha and J. Schmidhuber, “World models,” 2018. [Online]. Available: <https://zenodo.org/record/1207631>
- [17] R. S. Sutton, A. G. Barto et al., *Reinforcement learning: An introduction*. MIT press Cambridge, 1998, vol. 1, no. 1.
- [18] T. M. Moerland, J. Broekens, A. Plaat, and C. M. Jonker, “Model-based reinforcement learning: A survey,” 2022. [Online]. Available: <https://arxiv.org/abs/2006.16712>
- [19] D. Hafner, T. Lillicrap, J. Ba, and M. Norouzi, “Dream to control: Learning behaviors by latent imagination,” 2020. [Online]. Available: <https://arxiv.org/abs/1912.01603>
- [20] A. I. Károly, P. Galambos, J. Kuti, and I. J. Rudas, “Deep learning in robotics: Survey on model structures and training strategies,” *IEEE Transactions on Systems, Man, and Cybernetics: Systems*, vol. 51, no. 1, pp. 266–279, 2020.
- [21] G. E. Karniadakis, I. G. Kevrekidis, L. Lu, P. Perdikaris, S. Wang, and L. Yang, “Physics-informed machine learning,” *Nature Reviews Physics*, vol. 3, no. 6, pp. 422–440, 2021.
- [22] Z. Li, H. Zheng, N. Kovachki, D. Jin, H. Chen, B. Liu, K. Azizzadenesheli, and A. Anandkumar, “Physics-informed neural operator for learning partial differential equations,” 2023. [Online]. Available: <https://arxiv.org/abs/2111.03794>
- [23] M. Cranmer, S. Greydanus, S. Hoyer, P. Battaglia, D. Spergel, and S. Ho, “Lagrangian neural networks,” *arXiv preprint arXiv:2003.04630*, 2020.
- [24] S. Greydanus, M. Dzamba, and J. Yosinski, “Hamiltonian neural networks,” *Advances in neural information processing systems*, vol. 32, 2019.
- [25] F. J. Roth, D. K. Klein, M. Kannapinn, J. Peters, and O. Weeger, “Stable port-hamiltonian neural networks,” *Advances in Neural Information Processing Systems*, vol. 38, pp. 50 737–50 762, 2026.
- [26] P. Jin, Z. Zhang, A. Zhu, Y. Tang, and G. E. Karniadakis, “Symplectic: Intrinsic structure-preserving symplectic networks for identifying hamiltonian systems,” *Neural Networks*, vol. 132, pp. 166–179, 2020.
- [27] N. Hansen, H. Su, and X. Wang, “Td-mpc2: Scalable, robust world models for continuous control,” 2024.
- [28] A. van der Schaft, *L2-Gain and Passivity Techniques in Nonlinear Control*, 3rd ed. Cham, Switzerland: Springer International Publishing, 2017.
- [29] D. Kushwaha and Z. Biron, “A review on safe reinforcement learning using lyapunov and barrier functions,” *Artificial Intelligence Review*, vol. 59, no. 11611, 2026. [Online]. Available: <https://link.springer.com/article/10.1007/s10462-026-11611-9>
- [30] P. Vaidhyathanan, A. Papatheodorou, M. T. Mitchison, N. Ares, and I. Havoutis, “Metasym: A symplectic meta-learning framework for physical intelligence,” *arXiv preprint arXiv:2502.16667*, 2025.
- [31] M. M. Bronstein, J. Bruna, T. Cohen, and P. Velickovic, “Geometric deep learning: Grids, groups, graphs, geodesics, and gauges,” *CoRR*, vol. abs/2104.13478, 2021. [Online]. Available: <https://arxiv.org/abs/2104.13478>
- [32] Q. Hernández, A. Badías, D. González, F. Chinesta, and E. Cueto, “Structure-preserving neural networks,” *Journal of Computational Physics*, vol. 426, p. 109950, Feb. 2021. [Online]. Available: <http://dx.doi.org/10.1016/j.jcp.2020.109950>
- [33] S. Martinez, R. Griffin, and C. Mastalli, “Multi-contact inertial parameters estimation and localization in legged robots,” *IEEE Robotics and Automation Letters*, vol. 10, no. 5, pp. 4730–4737, 2025.
- [34] S. Martinez, S. Tonneau, and C. Mastalli, “System identification under constraints and disturbance: A bayesian estimation approach,” 2026. [Online]. Available: <https://arxiv.org/abs/2602.16358>
- [35] D. Ha and J. Schmidhuber, “Recurrent world models facilitate policy evolution,” *Advances in neural information processing systems*, vol. 31, 2018.
- [36] D. Hafner, T. Lillicrap, J. Ba, and M. Norouzi, “Dream to control: Learning behaviors by latent imagination,” *arXiv preprint arXiv:1912.01603*, 2019.
- [37] A. Sanchez-Gonzalez, J. Godwin, T. Pfaff, R. Ying, J. Leskovec, and P. Battaglia, “Learning to simulate complex physics with graph networks,” in *International conference on machine learning*. PMLR, 2020, pp. 8459–8468.
- [38] Z. Li, N. Kovachki, K. Azizzadenesheli, B. Liu, K. Bhattacharya, A. Stuart, and A. Anandkumar, “Fourier neural operator for parametric partial differential equations,” *arXiv preprint arXiv:2010.08895*, 2020.
- [39] Z. Li, D. Z. Huang, B. Liu, and A. Anandkumar, “Fourier neural operator with learned deformations for pdes on general geometries,” *Journal of Machine Learning Research*, vol. 24, no. 388, pp. 1–26, 2023.
- [40] C. Li, A. Krause, and M. Hutter, “Robotic world model: A neural network simulator for robust policy optimization in robotics,” 2025. [Online]. Available: <https://arxiv.org/abs/2501.10100>
- [41] P. Werbos, “Backpropagation through time: what it does and how to do it,” *Proceedings of the IEEE*, vol. 78, no. 10, pp. 1550–1560, 1990.
- [42] R. Pascanu, T. Mikolov, and Y. Bengio, “On the difficulty of training recurrent neural networks,” 2013. [Online]. Available: <https://arxiv.org/abs/1211.5063>
- [43] A. van der Schaft, *L2-Gain and Passivity Techniques in Nonlinear Control*, 3rd ed. Springer Publishing Company, Incorporated, 2018.
- [44] B. Maschke and A. van der Schaft, “Port-controlled hamiltonian systems: Modelling origins and systemtheoretic properties,” *IFAC Proceedings Volumes*, vol. 25, no. 13, pp. 359–365, 1992, 2nd IFAC

- Symposium on Nonlinear Control Systems Design 1992, Bordeaux, France, 24–26 June. [Online]. Available: <https://www.sciencedirect.com/science/article/pii/S1474667017523083>
- [45] P. J. Morrison, “Bracket formulation for irreversible classical fields,” *Physics Letters A*, vol. 100, no. 8, pp. 423–427, 1984. [Online]. Available: <https://www.sciencedirect.com/science/article/pii/0375960184906352>
- [46] H. Yoshimura and J. E. Marsden, “Dirac structures in lagrangian mechanics part i: Implicit lagrangian systems,” *Journal of Geometry and Physics*, vol. 57, pp. 133–156, 2006. [Online]. Available: <https://api.semanticscholar.org/CorpusID:5698662>
- [47] R. Abraham and J. Marsden, *Foundations of Mechanics*, ser. AMS Chelsea publishing. AMS Chelsea Pub./American Mathematical Society, 2008. [Online]. Available: <https://books.google.co.uk/books?id=4Y-ownk6ilsC>
- [48] M. Betancourt, M. I. Jordan, and A. C. Wilson, “On symplectic optimization,” *arXiv preprint arXiv:1802.03653*, 2018.
- [49] B. Igel'nik and N. Parikh, “Kolmogorov’s spline network,” *IEEE transactions on neural networks*, vol. 14, no. 4, pp. 725–733, 2003.
- [50] Z. Liu, P. Ma, Y. Wang, W. Matusik, and M. Tegmark, “Kan 2.0: Kolmogorov-arnold networks meet science,” *arXiv preprint arXiv:2408.10205*, 2024.
- [51] G. Buondonno and A. De Luca, “A recursive newton-euler algorithm for robots with elastic joints and its application to control,” in *2015 IEEE/RSJ International Conference on Intelligent Robots and Systems (IROS)*. IEEE, 2015, pp. 5526–5532.
- [52] R. Featherstone, “The calculation of robot dynamics using articulated-body inertias,” *The international journal of robotics research*, vol. 2, no. 1, pp. 13–30, 1983.
- [53] H. Goldstein, C. P. Poole, J. Safko *et al.*, *Classical mechanics*. Addison-wesley Reading, MA, 1950, vol. 2.
- [54] J. Solà, J. Deray, and D. Atchuthan, “A micro lie theory for state estimation in robotics,” 2021. [Online]. Available: <https://arxiv.org/abs/1812.01537>
- [55] V. Guillemin and S. Sternberg, *Symplectic techniques in physics*. Cambridge university press, 1990.
- [56] A. Weinstein, *Lectures on symplectic manifolds*. American Mathematical Soc., 1977, no. 29.
- [57] J. L. Koszul and Y. M. Zou, *Introduction to symplectic geometry*. Springer, 2019.
- [58] S. H. Strogatz, *Nonlinear Dynamics and Chaos: With Applications to Physics, Biology, Chemistry, and Engineering*, 2nd ed. CRC Press, 2018.
- [59] M. Hutter, C. Gehring, D. Jud, A. Lauber, C. D. Bellicoso, V. Tsounis, J. Hwangbo, K. Bodie, P. Fankhauser, M. Bloesch, R. Diethelm, S. Bachmann, A. Melzer, and M. Hoepflinger, “Anymal - a highly mobile and dynamic quadrupedal robot,” in *2016 IEEE/RSJ International Conference on Intelligent Robots and Systems (IROS)*, 2016, pp. 38–44.
- [60] A. Lamb, A. Goyal, Y. Zhang, S. Zhang, A. Courville, and Y. Bengio, “Professor forcing: A new algorithm for training recurrent networks,” 2016. [Online]. Available: <https://arxiv.org/abs/1610.09038>
- [61] X. Huang, Z. Li, G. He, M. Zhou, and E. Shechtman, “Self forcing: Bridging the train-test gap in autoregressive video diffusion,” 2025. [Online]. Available: <https://arxiv.org/abs/2506.08009>
- [62] B. K. Tapley, “Symplectic neural networks based on dynamical systems,” 2024. [Online]. Available: <https://arxiv.org/abs/2408.09821>
- [63] A. Gruber, K. Lee, H. Lim, N. Park, and N. Trask, “Efficiently parameterized neural metriplectic systems,” 2025. [Online]. Available: <https://arxiv.org/abs/2405.16305>
- [64] Y. D. Zhong, B. Dey, and A. Chakraborty, “Symplectic ODE-Net: Learning Hamiltonian Dynamics with Control,” *8th International Conference on Learning Representations, ICLR 2020*, 9 2019. [Online]. Available: <https://arxiv.org/abs/1909.12077v4>
- [65] N. Mohajerin, M. Mozifian, and S. Waslander, “Deep learning a quadrotor dynamic model for multi-step prediction,” in *2018 IEEE International Conference on Robotics and Automation (ICRA)*, 2018, pp. 2454–2459.
- [66] N. Mohajerin and S. L. Waslander, “Multistep prediction of dynamic systems with recurrent neural networks,” *IEEE Transactions on Neural Networks and Learning Systems*, vol. 30, no. 11, pp. 3370–3383, 2019.
- [67] Y. Fan, Z. Pei, C. Wang, M. Li, Z. Tang, and Q. Liu, “A review of quadruped robots: Structure, control, and autonomous motion,” *Advanced Intelligent Systems*, vol. 6, no. 6, p. 2300783, 2024.
- [68] J. Frey, T. Tuna, F. Fu, K. Patterson, T. Xu, M. Fallon, C. Cadena, and M. Hutter, “Grandtour: A legged robotics dataset in the wild for multi-modal perception and state estimation,” *arXiv preprint arXiv:2602.18164*, 2026.
- [69] L. Brunke, M. Greeff, A. W. Hall, Z. Yuan, S. Zhou, J. Panerati, and A. P. Schoellig, “Safe learning in robotics: From learning-based control to safe reinforcement learning,” 2021. [Online]. Available: <https://arxiv.org/abs/2108.06266>

APPENDIX A

AUTOREGRESSIVE ROLLOUT AND MULTI-HORIZON EVALUATION

The main experiments evaluate CALISYM autoregressively, with the model queried on its own predictions. Errors then compound along the horizon, which a one step metric cannot reveal. To characterize this, we roll out the same trained lifted predictor on the controlled dissipative double pendulum over horizons from 5 to 800 steps at a fixed $\Delta t = 0.01$ s (0.05 to 8.00 s), reporting in-distribution (ID) and out-of-distribution (OOD) mean-squared error (Table III).

The ID error stays small across the full sweep, rising from $\sim 10^{-5}$ at 5 steps to $\sim 10^{-2}$ at 800 steps with no runaway growth, so the lifted map remains numerically stable over an 8 s horizon despite the driven, dissipative dynamics. The OOD error grows steeply, as expected. Once a trajectory leaves the training distribution, each step is conditioned on an increasingly model generated state, compounding distribution shift error. The two effects are distinct. One is bounded numerical stability from the symplectic structure, and the other is error growth from distribution shift, rather than a single rollout failure.

TABLE III
ID AND OOD MULTI-HORIZON ROLLOUT ERROR.

Timesteps	ΔT [s]	ID MSE	OOD MSE
5	0.05	1.130×10^{-5}	0.070
10	0.10	2.616×10^{-5}	0.258
20	0.20	7.027×10^{-5}	0.718
50	0.50	2.478×10^{-4}	1.771
100	1.00	2.591×10^{-4}	4.892
200	2.00	6.396×10^{-4}	14.341
400	4.00	7.922×10^{-4}	39.553
600	6.00	0.033	69.460
800	8.00	0.033	101.397

APPENDIX B

SYMPLECTICITY CONSERVATION

The defining property of the learned lifted predictor is exact symplecticity in the lifted canonical phase space. For a differentiable map $\Phi_{\theta}^{\Delta t}$ on lifted coordinates \mathcal{Z} , symplecticity means

$$D\Phi_{\theta}^{\Delta t}(\mathcal{Z})^{\top} \mathbf{J}_{\Omega} D\Phi_{\theta}^{\Delta t}(\mathcal{Z}) = \mathbf{J}_{\Omega}, \quad (64)$$

where \mathbf{J}_{Ω} is the canonical symplectic matrix of the lifted space. GR-SYMPNET and GRB-SYMPNET satisfy this by construction, since each layer is the exact flow of a Hamiltonian system and the composition of symplectic maps remains symplectic.

We still verify the property numerically for the trained models (Table IV), for two reasons. First, it confirms that the trained architecture realizes the intended geometry rather than approximating it. Second, it separates a hard architectural constraint from a soft-regularization penalty, since a structurally

symplectic map sits at numerical precision regardless of the training loss, whereas a penalized one would track it. For each model we compute the normalized residual,

$$\epsilon_{\mathbf{J}_\Omega} = \frac{\|D\Phi_\theta^{\Delta t}(\mathbf{Z})^\top \mathbf{J}_\Omega D\Phi_\theta^{\Delta t}(\mathbf{Z}) - \mathbf{J}_\Omega\|_F}{\|\mathbf{J}_\Omega\|_F}. \quad (65)$$

The Jacobian is taken with respect to the lifted state \mathbf{Z} , not the projected physical state. This distinction is central to CALISYM, as the physical predictor induced by lifting, projecting, and embedding back is not required to be symplectic on the measured state. Symplecticity is enforced only on the lifted map.

TABLE IV
SYMPLECTICITY RESIDUALS ARE AT NUMERICAL PRECISION.

System	Architecture	Dim.	$\epsilon_{\mathbf{J}_\Omega}$ mean	$\epsilon_{\mathbf{J}_\Omega}$ max
Double pendulum	GRBSYMPNET	12	3×10^{-16}	4×10^{-15}
Quadrotor	GRSYMPNET	36	3×10^{-15}	8×10^{-15}
Quadruped	GRSYMPNET	132	5×10^{-16}	8×10^{-16}

APPENDIX C

UNIVERSAL APPROXIMATION OF GRB-SYMPNET

This appendix states the approximation property of the GRB-SYMPNET predictor used for compact low-dimensional lifted dynamics. The result is local in a canonical coordinate chart of the lifted phase space. This is the relevant setting for CALISYM, where symplecticity is imposed on the lifted map

$$\Phi_\theta^{\Delta t} : \mathcal{Z} \rightarrow \mathcal{Z},$$

while the induced physical predictor

$$\Pi_X \circ \Phi_\theta^{\Delta t} \circ \sigma_{\mathbf{e}_k} : X \rightarrow X$$

need not be symplectic on the measured physical state space $X := T^*Q$.

Let $\mathbf{Z} = (\mathbf{Q}, \mathbf{P}) \in \mathcal{Z} \simeq \mathbb{R}^{2d}$, with canonical symplectic form $\Omega = \sum_i dQ^i \wedge dP_i$ and canonical symplectic matrix \mathbf{J}_Ω . For a compact set $\mathcal{K} \subset \mathcal{Z}$, write $\|\cdot\|_{C^s(\mathcal{K})}$ for the maximum over derivatives up to order s . To avoid conflict with the auxiliary lifted coordinate \mathbf{r} , we denote the B-spline degree in this appendix by r_{spl} .

A GRB-SYMPNET layer is the exact generalized-ridge Hamiltonian flow

$$\begin{aligned} \xi_\ell &= \mathbf{A}_\ell \mathbf{P} + \mathbf{B}_\ell \mathbf{Q}, \\ \mathbf{Q}' &= \mathbf{Q} + h_\ell \mathbf{A}_\ell^\top \nabla K_\ell(\xi_\ell), \\ \mathbf{P}' &= \mathbf{P} - h_\ell \mathbf{B}_\ell^\top \nabla K_\ell(\xi_\ell), \\ \mathbf{A}_\ell \mathbf{B}_\ell^\top &= \mathbf{B}_\ell \mathbf{A}_\ell^\top. \end{aligned}$$

Equivalently, $\varphi_\ell(\mathbf{Q}, \mathbf{P}) = (\mathbf{Q}', \mathbf{P}')$. The scalar ridge Hamiltonian is parameterized as

$$\begin{aligned} K_\ell(\xi) &= K_{\ell, \text{spline}}(\xi) + K_{\ell, \text{smooth}}(\xi), \\ K_{\ell, \text{spline}}(\xi) &= \sum_{\alpha \in \mathcal{A}} c_{\ell, \alpha} \mathcal{B}_\alpha(\xi), \\ \mathcal{B}_\alpha(\xi) &= \prod_{j=1}^m B_{\alpha_j}^{(r_{\text{spl}})}(\xi_j). \end{aligned}$$

The smooth tail is

$$\begin{aligned} K_{\ell, \text{smooth}}(\xi) &= \sum_{j=1}^{N_s} a_{\ell j} \phi(\rho_{\ell j}), \\ \rho_{\ell j} &= \mathbf{w}_{\ell j}^\top \xi + b_{\ell j}. \end{aligned}$$

The smooth tail is useful in the experimental model class, but it is not needed for the density argument. Setting $K_{\ell, \text{smooth}} \equiv 0$ gives a subclass of the full GRB-SYMPNET family.

Theorem. *Lifted universal approximation by full-ridge GRB-SYMPNETs.* Let $\mathcal{U} \subset \mathcal{Z} \simeq \mathbb{R}^{2d}$ be open, let $\mathcal{K} \Subset \mathcal{U}$ be compact, and let $\Psi : \mathcal{U} \rightarrow \mathcal{Z}$ be a C^{s+1} symplectic map, meaning

$$\begin{aligned} D\Psi(\mathbf{Z})^\top \mathbf{J}_\Omega D\Psi(\mathbf{Z}) &= \mathbf{J}_\Omega, \\ \mathbf{Z} &\in \mathcal{U}. \end{aligned}$$

Assume that the generalized-ridge dimension may be chosen as $m = d$, and assume that the B-spline spaces used for $K_{\ell, \text{spline}}$ are C^{s+1} -dense on compact subsets of \mathbb{R}^d . For simple knots, it is sufficient to take $r_{\text{spl}} \geq s+2$. Then, for every $\varepsilon > 0$, there exists a finite-depth GRB-SYMPNET

$$\Phi_\theta^{\Delta t} = \varphi_L \circ \dots \circ \varphi_1$$

such that

$$\|\Phi_\theta^{\Delta t} - \Psi\|_{C^s(\mathcal{K})} < \varepsilon$$

and

$$\begin{aligned} D\Phi_\theta^{\Delta t}(\mathbf{Z})^\top \mathbf{J}_\Omega D\Phi_\theta^{\Delta t}(\mathbf{Z}) \\ = \mathbf{J}_\Omega. \end{aligned}$$

Thus GRB-SYMPNETs are dense, on compact subsets of the lifted canonical phase space, in the class of smooth symplectic maps, while remaining exactly symplectic for every parameter value.

a) Proof.: First, each GRB-SYMPNET layer is exactly symplectic. The layer is the time- h_ℓ flow of the scalar Hamiltonian

$$\begin{aligned} H_\ell(\mathbf{Q}, \mathbf{P}) &= K_\ell(\mathbf{A}_\ell \mathbf{P} + \mathbf{B}_\ell \mathbf{Q}) \\ &= K_\ell(\xi_\ell). \end{aligned}$$

Hamilton's equations give

$$\begin{aligned} \dot{\mathbf{Q}} &= \mathbf{A}_\ell^\top \nabla K_\ell(\xi_\ell), \\ \dot{\mathbf{P}} &= -\mathbf{B}_\ell^\top \nabla K_\ell(\xi_\ell). \end{aligned}$$

Hence

$$\begin{aligned} \dot{\xi}_\ell &= \mathbf{A}_\ell \dot{\mathbf{P}} + \mathbf{B}_\ell \dot{\mathbf{Q}} \\ &= (-\mathbf{A}_\ell \mathbf{B}_\ell^\top + \mathbf{B}_\ell \mathbf{A}_\ell^\top) \nabla K_\ell(\xi_\ell) \\ &= \mathbf{0}. \end{aligned}$$

Thus ξ_ℓ is constant along the layer flow. The Hamiltonian flow therefore integrates exactly to the explicit GRB layer above. Since exact Hamiltonian flows preserve Ω , each φ_ℓ is symplectic. The composition $\Phi_\theta^{\Delta t}$ is symplectic because symplectic maps are closed under composition.

It remains to prove density. In the full-ridge case $m = d$, the GRB layer contains the two standard gradient shears. For $(\mathbf{A}, \mathbf{B}) = (\mathbf{I}_d, \mathbf{0})$,

$$S_K^Q(\mathbf{Q}, \mathbf{P}) = (\mathbf{Q} + \nabla K(\mathbf{P}), \mathbf{P}).$$

For $(\mathbf{A}, \mathbf{B}) = (\mathbf{0}, \mathbf{I}_d)$,

$$S_{K_0}^P(\mathbf{Q}, \mathbf{P}) = (\mathbf{Q}, \mathbf{P} - \nabla K(\mathbf{Q})).$$

Let $K_0(\mathbf{u}) = \frac{1}{2} \|\mathbf{u}\|^2$. The canonical symplectic rotation

$$R(\mathbf{Q}, \mathbf{P}) = (\mathbf{P}, -\mathbf{Q})$$

factors as

$$R = S_{K_0}^P \circ S_{K_0}^Q \circ S_{K_0}^P.$$

Indeed, the three shears map (\mathbf{Q}, \mathbf{P}) to $(\mathbf{Q}, \mathbf{P} - \mathbf{Q})$, then to $(\mathbf{P}, \mathbf{P} - \mathbf{Q})$, and finally to $(\mathbf{P}, -\mathbf{Q})$.

For a scalar potential $V : \mathbb{R}^d \rightarrow \mathbb{R}$ and a constant vector $\boldsymbol{\eta} \in \mathbb{R}^d$, define the Hénon-like symplectic map

$$H_{V, \boldsymbol{\eta}}(\mathbf{Q}, \mathbf{P}) = (\mathbf{P} + \boldsymbol{\eta}, -\mathbf{Q} + \nabla V(\mathbf{P})).$$

It is represented using GRB shears by

$$H_{V, \boldsymbol{\eta}} = T_{\boldsymbol{\eta}}^Q \circ R \circ S_{-V}^Q,$$

$$T_{\boldsymbol{\eta}}^Q(\mathbf{Q}, \mathbf{P}) = (\mathbf{Q} + \boldsymbol{\eta}, \mathbf{P}).$$

The translation $T_{\boldsymbol{\eta}}^Q$ is generated by the linear potential $K(\mathbf{P}) = \boldsymbol{\eta}^\top \mathbf{P}$, while the rotation is generated by quadratic shear potentials. These linear and quadratic potentials are contained in, or can be approximated arbitrarily well by, the spline Hamiltonian class on compact sets.

By the Hénon approximation theorem for symplectic maps, and by the same approximation route underlying SympNet universality [26], there exist smooth scalar potentials V_1, \dots, V_N and constant vectors $\boldsymbol{\eta}_1, \dots, \boldsymbol{\eta}_N$ such that

$$\mathcal{H} = H_{V_N, \boldsymbol{\eta}_N} \circ \dots \circ H_{V_1, \boldsymbol{\eta}_1},$$

$$\|\Psi - \mathcal{H}\|_{C^s(\mathcal{K})} < \frac{\varepsilon}{2}.$$

Let \mathcal{K}_j be compact neighborhoods of the image sets encountered by this finite composition, and let π_P denote projection onto the \mathbf{P} -coordinates. Since the spline Hamiltonian class is C^{s+1} -dense, choose spline potentials $K_{j,G}$ such that

$$\|V_j - K_{j,G}\|_{C^{s+1}(\pi_P \mathcal{K}_j)} < \delta_j.$$

Because $H_{V_j, \boldsymbol{\eta}_j}$ depends on V_j only through ∇V_j , there is a compact-set constant C_j with

$$\|H_{V_j, \boldsymbol{\eta}_j} - H_{K_{j,G}, \boldsymbol{\eta}_j}\|_{C^s(\mathcal{K}_j)} \leq C_j \delta_j.$$

Define the spline-composed Hénon approximation

$$\tilde{\mathcal{H}}_G = H_{K_{N,G}, \boldsymbol{\eta}_N} \circ \dots \circ H_{K_{1,G}, \boldsymbol{\eta}_1}.$$

Continuity of finite composition in the C^s topology allows the δ_j to be chosen so that

$$\|\mathcal{H} - \tilde{\mathcal{H}}_G\|_{C^s(\mathcal{K})} < \frac{\varepsilon}{2}.$$

The map $\tilde{\mathcal{H}}_G$ is a GRB-SYMPNET because each Hénon-like factor is built from GRB shears with spline scalar Hamiltonians. Hence the resulting network satisfies

$$\|\Phi_{\theta}^{\Delta t} - \Psi\|_{C^s(\mathcal{K})} < \varepsilon.$$

Exact symplecticity follows from the layer construction.

b) *Spline-rate form.*: After fixing a Hénon approximation

$$\mathcal{H} = H_{V_N, \boldsymbol{\eta}_N} \circ \dots \circ H_{V_1, \boldsymbol{\eta}_1},$$

the usual spline approximation rate gives a quantitative version of the preceding argument. If each V_j has sufficient smoothness on the relevant compact set and the spline grid for V_j has G_j intervals in each ridge coordinate, then

$$\|\Psi - \Phi_{\theta, G}^{\Delta t}\|_{C^s(\mathcal{K})} \leq \varepsilon_{\text{Hénon}} + C_{\text{comp}} \sum_{j=1}^N G_j^{-(r_{\text{spl}}-s)}.$$

Here $\varepsilon_{\text{Hénon}} = \|\Psi - \mathcal{H}\|_{C^s(\mathcal{K})}$ is the finite Hénon-composition error, and C_{comp} depends on the compact image chain and derivative bounds of the composed maps. The loss of one derivative is intrinsic: the symplectic layer uses ∇K_ℓ , so C^s approximation of the map requires C^{s+1} approximation of the scalar Hamiltonian.

c) *Fixed-ridge interpretation.*: The theorem above is a full-ridge universal approximation result, since it allows $m = d$. The practical GRB-SYMPNET regime may use $m \ll d$ for parameter efficiency. In that case, the corresponding statement is ridge-structured rather than fully universal. Suppose the generating potentials in the Hénon approximation admit additive generalized-ridge structure,

$$V_j(\mathbf{P}) = \sum_{\nu=1}^{R_j} W_{j,\nu}(\mathbf{C}_{j,\nu} \mathbf{P}), \quad \mathbf{C}_{j,\nu} \in \mathbb{R}^{m \times d}.$$

Then

$$\nabla V_j(\mathbf{P}) = \sum_{\nu=1}^{R_j} \mathbf{C}_{j,\nu}^\top \mathbf{g}_{j,\nu}(\mathbf{P}),$$

$$\mathbf{g}_{j,\nu}(\mathbf{P}) = \nabla W_{j,\nu}(\mathbf{C}_{j,\nu} \mathbf{P}).$$

Each summand is exactly the update produced by a GRB layer with $\mathbf{A} = \mathbf{C}_{j,\nu}$ and $\mathbf{B} = \mathbf{0}$:

$$\mathbf{Q}' = \mathbf{Q} + \mathbf{C}_{j,\nu}^\top \nabla W_{j,\nu}(\mathbf{C}_{j,\nu} \mathbf{P}),$$

$$\mathbf{P}' = \mathbf{P}.$$

Because these layers leave \mathbf{P} fixed, their composition adds the ridge-gradient contributions. The same argument applies to \mathbf{P} -shears. Thus, for $m \ll d$, GRB-SYMPNET is universal for the class of symplectic maps whose scalar generating potentials admit smooth low-dimensional generalized-ridge decompositions. This is the regime targeted by the low-dimensional double-pendulum experiment, where the spline ridge parameterization remains compact.

d) *Induced physical predictor.*: The lifted result directly implies an approximation statement for the CALISYM physical predictor. Let $C_X \Subset X$ and $C_E \Subset E$ be compact sets of physical states and ports. Suppose the one-step physical transition

$$f : X \times E \rightarrow X, \quad f(\mathbf{x}, \mathbf{e}) = f_{\mathbf{e}}(\mathbf{x}),$$

admits a smooth lifted symplectic realization on the data section. That is, assume there exists a C^{s+1} symplectic map Ψ such that

$$f_{\mathbf{e}}(\mathbf{x}) = \Pi_X(\Psi(\sigma_{\mathbf{e}}(\mathbf{x}))),$$

$$(\mathbf{x}, \mathbf{e}) \in C_X \times C_E.$$

Let

$$\mathcal{K}_S = \{\sigma_{\mathbf{e}}(\mathbf{x}) : \mathbf{x} \in C_X, \mathbf{e} \in C_E\} \subset \mathcal{Z}.$$

By the theorem, Ψ can be approximated in C^s on a compact neighborhood of \mathcal{K}_S by a GRB-SYMPNET $\Phi_{\theta}^{\Delta t}$. Define the induced physical predictor

$$\widehat{f}_{\theta, \mathbf{e}} = \Pi_X \circ \Phi_{\theta}^{\Delta t} \circ \sigma_{\mathbf{e}}.$$

Then, for every $\varepsilon > 0$, there exists a GRB-SYMPNET lifted predictor such that

$$\sup_{\mathbf{e} \in C_E} \|\widehat{f}_{\theta, \mathbf{e}} - f_{\mathbf{e}}\|_{C^s(C_X)} < \varepsilon.$$

At the same time, the lifted map remains exactly symplectic:

$$D\Phi_{\theta}^{\Delta t}(\mathbf{Z})^{\top} \mathbf{J}_{\Omega} D\Phi_{\theta}^{\Delta t}(\mathbf{Z}) = \mathbf{J}_{\Omega}.$$

This formalizes the modeling principle used throughout CALISYM. The projected physical dynamics may be forced, dissipative, or contact-rich, while the learned map in the lifted canonical coordinates remains exactly symplectic.

A sufficient local condition for the lifted-realization assumption is that the joint map

$$F(\mathbf{x}, \mathbf{e}) = (f_{\mathbf{e}}(\mathbf{x}), \mathbf{e})$$

is a local diffeomorphism. In the base–fiber coordinates used by the lift,

$$\begin{aligned} \mathbf{b} &= (\mathbf{q}, \mathbf{p}, \boldsymbol{\mu}_u, \boldsymbol{\lambda}_c), \\ \boldsymbol{\zeta} &= (\mathbf{r}, -\mathbf{y}, -\boldsymbol{\lambda}_u, \boldsymbol{\pi}_c), \\ \Omega &= \sum_i db^i \wedge d\zeta_i, \end{aligned}$$

the cotangent lift T^*F is symplectic and recovers the physical transition after projection to the gauge-fixed data section. This is why CALISYM can impose symplecticity in \mathcal{Z} without requiring the projected map on X to be symplectic.

e) KAN interpretation.: The B-spline/KAN-style approximation is applied to the scalar ridge Hamiltonians K_{ℓ} , not componentwise to the vector-valued map $\mathbf{Z} \mapsto \Phi_{\theta}^{\Delta t}(\mathbf{Z})$. This distinction is essential: componentwise approximation does not preserve

$$D\Phi^{\top} \mathbf{J}_{\Omega} D\Phi = \mathbf{J}_{\Omega}.$$

In GRB-SYMPNET, the learned spline functions enter only through scalar Hamiltonians inside exact generalized-ridge flows, so expressivity is added without breaking the symplectic constraint.

APPENDIX D TRAINING DETAILS

A. Double pendulum training

1) *Hyperparameters:* Table V gives the configuration for the double pendulum, the low dimensional setting for the spline variant GRB-SYMPNET. The lifted phase space is 12 dimensional and the model is small, 3,660 parameters over 12 layers. The scalar ridge Hamiltonian uses a cubic B-spline over 12 intervals on $[-3.5, 3.5]$, evaluated in a projection dimension $m = 2$, which adds compact local expressivity in the ridge coordinate without breaking the exact symplectic

flow. Training runs in FP64 with AdamW for 500 epochs. The loss emphasizes the physical state ($w_q = 10$, $w_p = 5$) with a single control port ($w_{\mu} = 5$), since the pendulum is isolated with one torque port and no contacts.

2) *Data Preparation:* Unlike the quadraped and quadrotor benchmarks, which are derived from real-world datasets, the double-pendulum benchmark is generated directly from a known physical model. The system consists of a two-link planar pendulum subject to gravity, viscous damping, and external control torques. Trajectories are produced by numerically integrating the equations of motion using a high-order DOP853 integrator with zero-order-hold control inputs, yielding a controlled dissipative mechanical system with known ground-truth dynamics.

The state is represented using joint angles and generalized momenta. Since the configuration space is Euclidean, no manifold preprocessing is required. Control inputs are generated independently for each joint using randomized sinusoidal torque profiles, producing a diverse set of excitation patterns. Trajectories are generated directly at 100 Hz and segmented into overlapping windows of 100 time steps (1 s) with a stride of 10 samples, resulting in approximately 40,000 training windows and 1,600 OOD windows.

To evaluate out-of-distribution generalization, the train and OOD splits are constructed using the system’s total mechanical energy rather than a random partition of trajectories. OOD episodes are initialized in an energy regime approximately 36% higher than that used for training, creating a physically meaningful distribution shift. Since mechanical energy directly governs the amplitude of motion, nonlinear coupling strength, and overall complexity of the resulting dynamics, higher-energy trajectories explore larger regions of phase space and exhibit qualitatively different long-horizon behavior than those observed during training.

Importantly, the distribution shift persists beyond the initial conditions. Although viscous friction continuously dissipates energy throughout each rollout, OOD trajectory windows exhibit approximately 56% higher mean mechanical energy than training windows and consistently occupy more energetic regions of phase space throughout their evolution. Consequently, the benchmark evaluates generalization across distinct dynamical regimes and trajectory families rather than simple interpolation between nearby samples, yielding a substantially more challenging and physically grounded OOD evaluation protocol than conventional random trajectory splits.

B. Quadrotor training

1) *Hyperparameters:* Table V gives the configuration for the quadrotor, the forced underactuated setting for GRB-SYMPNET without contact ports. The lifted phase space is 36 dimensional, realized with 23,688 parameters. The lift embeds the rotor thrust and body torque commands as a single control port, so the contact block is omitted and energy enters only through actuation while drag acts as unmodeled dissipation. Training runs in FP64 with AdamW at a constant learning rate of 3×10^{-3} for 500 epochs, using a teacher forcing schedule held at $\alpha = 1.0$ for 50 epochs followed by a 50 epoch linear

ramp. The loss emphasizes the physical state ($w_q = w_p = 10$) with light section and port weights ($w_{\text{sec}} = w_\mu = 0.1$), in contrast to the heavily port weighted quadruped objective, since the quadrotor has a single smooth actuation channel rather than several heterogeneous ports.

2) *Data Preparation*: We evaluate the quadrotor experiments on the AscTec Pelican Flight Dataset [65], [66], which contains 54 real-world flight trajectories collected on an AscTec Pelican platform. Unlike the quadruped, the quadrotor is a single free-flying rigid body without articulated joints or contacts, resulting in a substantially simpler preprocessing pipeline. The dataset provides pose, velocities, body rates, and motor commands at 100 Hz. Each trajectory is expressed in local tangent-space coordinates by applying the logarithm map on $\mathbb{SE}(3)$ relative to the initial pose of each window, yielding a six-dimensional configuration vector $\mathbf{q} \in \mathbb{R}^6$.

Generalized momenta are computed as $\mathbf{p} = \mathbf{M}\mathbf{v}$ using the constant rigid-body mass matrix $\mathbf{M} = \text{diag}(m\mathbb{I}_3, \mathbf{I}_{\text{body}})$. Control inputs are represented as generalized wrenches obtained by mapping the four motor commands through the quadrotor allocation matrix, yielding $\boldsymbol{\tau} \in \mathbb{R}^6$.

The trajectories require no resampling or filtering and are segmented into overlapping windows of 100 time steps (1 s) with a stride of 10 samples. After a momentum-smoothness validation step removes anomalous segments, the resulting data are split into disjoint training and OOD flight sets to evaluate generalization to previously unseen trajectories.

C. Quadruped training

1) *Hyperparameters*: Table V gives the configuration for the quadruped, the high dimensional contact rich setting for GR-SYMPNET. The lifted phase space is 132 dimensional, realized with $\sim 316\text{K}$ parameters over 18 layers of width 66. The generalized-ridge layers confine the nonlinear computation to a low dimensional ridge coordinate, which keeps the predictor parameter efficient despite the large phase space. Training runs in FP64 with Muon for 500 epochs. The loss weights the control and contact ports heavily ($w_\mu = 65$, $w_{f_c} = 55$) against an equal state weighting ($w_q = w_p = 0.5$) and a light section penalty ($w_{\text{sec}} = 0.01$). The heavy port weighting is the channel through which actuation work and contact impulses enter an otherwise conservative lifted flow.

2) *Data Preparation*: The GRANDTOUR dataset [68] comprises diverse real-world locomotion trajectories collected on the ANYmal-D quadruped [59] across a wide range of terrains, commands, gaits, and environmental conditions. The onboard state-estimation stack provides measurements at 400 Hz. To construct a dataset compatible with the proposed lifted formulation, the raw estimator outputs are transformed into a canonical mechanical state representation and subsequently filtered, resampled, and validated.

The quadruped configuration consists of an $\mathbb{SE}(3)$ floating-base pose together with Euclidean joint coordinates. Since only the floating base evolves on a nonlinear manifold, each trajectory window is expressed relative to its initial base pose using the $\mathbb{SE}(3)$ logarithm map implemented in Pinocchio, while the joint coordinates remain unchanged. Generalized

momenta are then computed from the rigid-body dynamics model yielding the canonical state representation (\mathbf{q}, \mathbf{p}) used throughout this work.

The resulting trajectories are resampled from 400 Hz to 100 Hz. Prior to decimation, the momentum channels are filtered using an 18 Hz sixth-order low-pass filter. Given the target Nyquist frequency of 50 Hz, this removes high-frequency transients arising from impacts, contact transitions, and estimator noise while preserving the dominant locomotion dynamics, which typically lie below 10 Hz. This prevents aliasing artifacts from contaminating the momentum channels after downsampling.

Finally trajectories are segmented into overlapping windows of 100 time steps (1 s) with a stride of 10 samples. A validation stage rejects windows exhibiting anomalous momentum discontinuities, and the remaining data are partitioned into disjoint training and OOD mission sets to evaluate generalization across previously unseen operating conditions.

TABLE V
TRAINING CONFIGURATIONS FOR THE DOUBLE PENDULUM, QUADROTOR, AND QUADRUPEDED EXPERIMENTS.

	Double Pend.	Quadrotor	Quadruped
Architecture			
SYMPNET type	GRB	GR	GR
Phase-space dim.	12	36	132
Parameters	3,660	23,688	316,008
Layers (L)	12	14	18
Width (W)	–	36	66
Activation	–	tanh	tanh
Projection dimension	2	–	–
Spline degree	3	–	–
Spline intervals	12	–	–
Knot range	$[-3.5, 3.5]$	–	–
Backbone hidden dim.	8	–	–
Dataset			
Training windows	40,000	98,552	126,309
ID test windows	1,000	24,638	31,577
OOD test windows	1,600	15,129	14,780
Sampling period (δt) [s]	0.01	0.01	0.01
Evaluation horizon (ΔT)	200 (2s)	100 (1s)	100 (1s)
Training			
Optimizer	AdamW	AdamW	Muon
Learning rate	5×10^{-3}	3×10^{-3}	10^{-2}
Weight decay	2×10^{-4}	10^{-3}	10^{-3}
Gradient clipping	100	100	500
Precision	FP64	FP64	FP64
Epochs	500	500	500
Batch size	1024	1024	2048
TF training horizon	100	100	100
Loss Weights			
Configuration (w_q)	10.0	10.0	0.5
Momentum (w_p)	5.0	10.0	0.5
Section (w_{sec})	5.0	0.01	0.01
Control port (w_μ)	5.0	0.1	65.0
Contact port (w_{f_c})	–	–	55.0
Symplectic normalization	Enabled	Enabled	Enabled